

**Master's Thesis**

**Feasibility study for measurement of  
beta-decay rates of  $\Lambda$  hypernuclei**

**Kento Kamada**

**Department of Physics  
Graduate School of Science  
Tohoku University  
2021**



# Abstract

It has been discussed that the baryon properties can be modified in nuclear medium. Experimentally, only the EMC effect indicates the baryon modification in nuclear matter, but its mechanism has not been clearly explained. We consider that the baryon modification can be clarified by measuring the beta decay of  $\Lambda$  hypernucleus. We expect that a  $\Lambda$  is swelled since u and d quark wavefunctions are affected by the meson field in a nucleus. If it is true, when  $\Lambda$ 's beta decay takes place, the spatial overlap of the initial state s quark and the final state u quark wavefunctions may be reduced comparing with that in the free space. This change of the baryon structure can be detected by measuring the beta decay rate of a  $\Lambda$  in a nucleus. According to a calculation by Quark Meson Coupling model, the structure change makes the axial charge  $g_A$  of a  $\Lambda$  reduced by 10% at maximum in the nuclear density of  $0.17 \text{ fm}^{-3}$ , and then the  $\Lambda$ 's beta decay rate decreases by 20% at maximum.

To clearly measure a change of the beta decay rate by baryon modification, the other effects (nuclear many-body effects and hadronic effects) should be small. Since these effects are expected to be small for light nuclei, we will use  ${}^5_\Lambda\text{He}$  hypernucleus for the beta decay measurement. We plan to carry out an experiment at the J-PARC K1.1 beamline, in which  ${}^5_\Lambda\text{He}$  will be produced via the  ${}^6\text{Li}(\pi^+, K^+){}^6_\Lambda\text{Li}$  reaction. Since we want to measure the beta decay rate within 4.5% accuracy, the branching ratio of the beta decay and the lifetime of  ${}^5_\Lambda\text{He}$  should be measured within 4% and 2% accuracy, respectively. In the case of the  ${}^5_\Lambda\text{He}$  lifetime, it was previously measured with 4% accuracy in the KEK E462 experiment by using the same  $(\pi^+, K^+)$  reaction. We will use almost the same setup as the KEK E462 experiment and achieve 2% accuracy. In the case of the branching ratio, no measurement has been carried out yet. Since the branching ratio of the  $\Lambda$ 's beta decay ( $\sim 8.0 \times 10^{-4}$ ) is much smaller than that of the  $\Lambda$ 's main decay modes ( $\Lambda \rightarrow n\pi^0$  and  $\Lambda \rightarrow p\pi^-$ ), huge background from  $\pi^0$  and  $\pi^-$  is expected to be a severe problem for measuring the beta decay events. The background counts should be of the order of 1% of the beta decay electron counts. We designed detectors around the target. A  ${}^6\text{Li}$  target is surrounded by plastic counters, lucite Cerenkov counters and a BGO calorimeter. The plastic counters identify charged particles, the lucite Cerenkov counters distinguish the beta decay electron from other charged particles and the BGO calorimeter measures the energy of the beta decay electron. We made simulations to develop background suppression methods and show feasibility of the beta decay measurement by using GEANT4 simulation code. In the analysis in a BGO calorimeter, by selecting one-cluster

hit events as the beta decay electron, 97% of  $\pi^0$  and 92.8% of  $\pi^-$  can be rejected. In the analysis in the plastic counter, by selecting a MIP peak region in the energy loss, 88% of  $\pi^0$  and 99.9% of  $\pi^-$  can be rejected. In addition, 95.5% of  $\pi^-$  and 90% of  $\pi^0$  are rejected by the Lucite Cerenkov counter. Via the background suppression study, the background rate per beta decay electron signal is reduced down to 4%.

Using the yield and the accuracy of the KEK E462 experiment, it is estimated that the branching ratio and the lifetime can be measured with 4% and 2% statical errors in 1400 hours and 120 hours of beam time, respectively. The background will be significantly suppressed and give about 3% systematic error. Therefore, this beta decay experiment is found to be feasible. Most of the present results have been reported as a Letter-Of-Intent to J-PARC. In near future, we will make more realistic simulation considering the energy resolution of the BGO.

# Contents

<b>1 Introduction</b> .....	1
1.1 Modification of $\Lambda$ 's beta decay in nuclear matter.....	1
1.2 Change of $g_A$ by QMC model.....	3
1.3 $\Lambda$ 's weak decay.....	5
<b>2 Experiment for measuring the <math>\Lambda</math>'s beta-decay rate</b> .....	8
2.1 Modification of $\Lambda$ in ${}^5_\Lambda\text{He}$ .....	8
2.2 Production of ${}^5_\Lambda\text{He}$ at J-PARC K1.1 beamline.....	9
2.2.1 Via the $(\pi^+, K^+)$ or $(K^-, \pi^-)$ reaction? .....	1 0
2.2.2 K1.1 beamline spectrometer .....	1 0
2.2.3 SKS spectrometer .....	1 2
2.2.4 ${}^6\text{Li}$ target .....	1 2
2.3 Apparatus around the target for measuring.....	1 3
2.4 Detectors around the Li target.....	1 4
2.4.1 BGO calorimeter .....	1 4
2.4.2 Plastic counter .....	1 5
2.4.3 Lucite Cerenkov counter .....	1 5
2.5 Setup for measuring the lifetime .....	1 6
<b>3 Background reduction study for the branching ratio</b> .....	1 8
3.1 Principles of background suppression and simulations.....	1 8
3.2 $\pi^0$ and $\pi^-$ background study .....	2 0
3.2.1 Cluster analysis in BGO counter .....	2 1
3.2.2 Analysis in the plastic counter .....	2 2
3.2.3 Analysis in lucite Cerenkov counter .....	2 5
3.2.4 Correlation between hit positions of detectors.....	2 5
3.2.5 Photon detector around the SKS spectrometer.....	2 7
3.2.6 Spectrum of beta decay electron.....	2 7
3.3 Optimization of BGO counter.....	2 9
3.3.1 Optimization of the number of segments of BGO .....	2 9
3.3.2 Optimization of the thickness of BGO .....	3 1
3.4 Optimization of the photon veto counter in SKS .....	3 2

3.5 Study of other background.....	3 4
3.5.1 Nonmesonic weak decay of $\Lambda$ .....	3 4
3.5.2 Reduction of nonmesonic weak decay of $\Lambda$ .....	3 4
3.5.3 $\mu^-$ from three body decay of $\Lambda$ .....	3 7
3.5.4 Quasi-free $\Lambda$ .....	3 8
3.5.5 Reduction of quasi-free $\Lambda$ .....	4 3
3.6 Effects from beam $\pi^+$ .....	4 7
<b>4 Feasibility of the beta decay experiment .....</b>	<b>4 9</b>
4.1 Yield and accuracy of branching ratio of beta decay.....	4 9
4.2 Yield and accuracy of lifetime.....	5 0
<b>5 Summary and future prospect.....</b>	<b>5 1</b>
Appendix A.....	5 3
A.1 Beta decay theory .....	5 3
A.2 Beta decay model under V–A .....	5 5
A.3 $g_V$ and $g_A$ values .....	5 6
Appendix B.....	5 7
B.1 J-PARC.....	5 7
B.2 J-PARC Hadron Experimental Facility .....	5 8
B.3 J-PARC K1.1 beamline.....	5 8
Appendix C.....	6 0
C.1 $\Lambda \rightarrow n\gamma$ decay rate in nuclear matter.....	6 0
C.2 Cluster analysis in the BGO calorimeter .....	6 1
C.3 Analysis in the plastic counters .....	6 1
C.4 Analysis of the total energy deposit in BGO.....	6 2
C.5 Summary .....	6 2

## List of Figures

1.1 Schematic view of the beta decay of a $\Lambda$ baryon in the free space and in a nucleus...	2
1.2 Change of the axial vector charge $g_A$ of a $\Lambda$ in nuclear density $\rho$ predicted by QMC model .....	3
1.3 Decay branching ratios of a $\Lambda$ in the free space .....	5
1.4 Kinetic energy spectra of $\pi^-$ and $\pi^0$ from ${}^5_\Lambda\text{He}$ calculated by Motoba .....	6
1.5 The total energy of neutron-proton pair and neutron-neutron pair from ${}^5_\Lambda\text{He}$ weak decay measured in the KEK E462 experiment .....	6
1.6 The kinetic energy spectra of the beta decay electron from $\Lambda \rightarrow p e^- \bar{\nu}_e$ decay .....	7
2.1 The quenching effect of the axial vector charge $g_A$ for beta decay of various light nuclei .....	8
2.2 Experimental setup for measuring the beta decay rate at J-PARC K1.1 beamline ....	9
2.3 The excitation energy spectrum of the ${}^6_\Lambda\text{Li}$ by the $(\pi^+, K^+)$ reaction measured in the KEK E462 experiment .....	11
2.4 The excitation energy spectrum of the ${}^6_\Lambda\text{Li}$ by the $(K^-, \pi^-)$ reaction .....	11
2.5 Schematic view of the setup for measuring the branching ratio .....	14
2.6 A schematic view of the expected setup around the target for the lifetime measurement .....	17
2.7 The decay time spectra for ${}^5_\Lambda\text{He}$ and ${}^{12}_\Lambda\text{C}$ measured in the KEK E462 experiment ...	17
3.1 An illustration of events of the beta decay electron as well as $\pi^0$ and $\pi^-$ from the $\Lambda$ 's main decay modes .....	19
3.2 Apparatus around the target in the present GEANT4 simulation .....	20
3.3 The number of clusters in BGO for the beta decay electron, $\pi^0$ and $\pi^-$ from ${}^5_\Lambda\text{He}$ decay in the simulation .....	21
3.4 Examples of simulated hit patterns in BGO segments for the beta decay electron, $\pi^0$ and $\pi^-$ events .....	21
3.5 The total energy deposit in the plastic counter for the beta decay electron, $\pi^0$ and $\pi^-$ in the simulation .....	22
3.6 Schematic view of the detectors around the Li target .....	23
3.7 Simulated 2D plot of the total energy deposit and the path length in the plastic counter for $\pi^0$ and the beta decay electron .....	24
3.8 The energy deposit per path length in the plastic counter for the beta decay electron, $\pi^0$ and $\pi^-$ in the simulation .....	24

3.9 Schematic views of a beta decay electron event and a misidentified $\pi^0$ event in the simulation .....	26
3.10 Difference of the z positions between points A and C for the beta decay electron and $\pi^0$ in the simulation .....	26
3.11 The expected photon veto counters to be installed around the SKS magnet .....	27
3.12 Simulated spectrum of the beta decay electron energy and the remaining background events after all the background reduction analysis .....	28
3.13 Simulated background rate for the beta decay electron as a function of the number of BGO segments .....	29
3.14 An example of the hit pattern of beta decay electron, $\pi^0$ and $\pi^-$ in the case of 225 BGO segments in the simulation .....	30
3.15 An example of the hit pattern of beta decay electron, $\pi^0$ and $\pi^-$ in the case of 49 BGO segments in the simulation .....	30
3.16 The number of clusters in the BGO for the beta decay electron, $\pi^0$ and $\pi^-$ in the case of 49 segments (simulation) .....	30
3.17 Simulated background rate of the beta decay electron as a function of the BGO thickness .....	31
3.18 An example of the simulated hit pattern in the BGO calorimeter for $\pi^-$ in the case of 10 cm and 30cm BGO thickness .....	32
3.19 The relation between the detection rate of 100 MeV photon and the thickness of the lead (5 mm ~ 15 mm) in the case of one-layer structure (simulation) .....	33
3.20 Measured angle between neutron-proton pair and neutron-neutron pair in the KEK E462 experiment .....	34
3.21 The number of clusters in BGO for $\Lambda p \rightarrow np$ and $\Lambda n \rightarrow nn$ in the simulation .....	35
3.22 The total energy deposit in the plastic counter for $\Lambda p \rightarrow np$ and $\Lambda n \rightarrow nn$ in the simulation .....	35
3.23 The energy deposit per path length in the plastic counter for $\Lambda p \rightarrow np$ and $\Lambda n \rightarrow nn$ after selecting 0.7 – 3 MeV as the beta decay electron in the total energy deposit (simulation) .....	36
3.24 Simulated energy spectra in BGO of remaining $\Lambda p \rightarrow np$ and $\Lambda n \rightarrow nn$ events .....	36
3.25 Calculated spectra of the kinetic energy and the velocity of muons in the $\Lambda \rightarrow pe^- \bar{\nu}_\mu$ decay .....	37
3.26 Missing mass spectra of production of ${}^6_\Lambda\text{Li}$ and quasi-free $\Lambda$ (Q-F $\Lambda$ ) .....	38
3.27 Schematic view of quasi-free $\Lambda$ (Q-F $\Lambda$ ) production .....	38

3.28	The momentum distribution of the neutron in $^{12}\text{C}$ measured by $^{12}\text{C}(e, e'p)$ reaction .....	39
3.29	$\pi^+n \rightarrow K^+\Lambda$ reaction in the Lab and the CM systems .....	40
3.30	Calculated momentum distributions of Q-F $\Lambda$ for x, y, z directions .....	41
3.31	Calculated distributions of $\Lambda$ 's generation points for x, y, z directions .....	41
3.32	The excitation energy of calculated Q-F $\Lambda$ .....	42
3.33	Calculated momentum distributions of Q-F $\Lambda$ for x, y, z directions after selecting $-5 \text{ MeV} \leq E_{\text{ex}} \leq 5 \text{ MeV}$ .....	42
3.34	Calculated distributions of $\Lambda$ 's generation points for x, y, z directions after selecting $-5 \text{ MeV} \leq E_{\text{ex}} \leq 5 \text{ MeV}$ .....	42
3.35	The hit pattern and the number of clusters in BGO for Q-F $\Lambda$ in the simulation ...	43
3.36	The total energy deposit in the plastic counter for Q-F $\Lambda$ in the simulation .....	44
3.37	The energy deposit per path length in the plastic counter for Q-F $\Lambda$ after selecting $0.7 - 3 \text{ MeV}$ as the beta decay electron in the total energy deposit .....	44
3.38	Simulated energy spectrum in BGO of remaining Q-F $\Lambda$ events .....	45
3.39	The theta segment number of the center of one-cluster in the BGO .....	46
3.40	BGO counting rate with more than 1 MeV as a function of segment theta number in the simulation .....	47
3.41	Fraction of the number of BGO segments with more than $10^3$ counts (n) out of all the BGO segments of 225 (N) as a function of the energy threshold in the simulation .....	48
3.42	Fraction of the number of BGO segments with more than $10^3$ counts (n) out of all the BGO segments of 225 (N) as a function of the number of BGO segments in the simulation .....	48
B.1	A schematic view of J-PARC .....	57
B.2	A schematic view of the J-PARC Hadron Experimental Facility .....	58
B.3	A schematic view of the K1.1 beamline at the J-PARC Hadron Experimental Facility .....	59
C.1	A diagram of $\Lambda \rightarrow n\gamma$ decay .....	60
C.2	The number of clusters in the BGO for $\Lambda \rightarrow n\gamma$ , $\pi^0$ and $\pi^-$ in the simulation .....	61
C.3	The total energy deposit in the plastic counter for $\Lambda \rightarrow n\gamma$ , $\pi^0$ and $\pi^-$ in the simulation .....	61
C.4	The total energy deposit in the BGO for $\Lambda \rightarrow n\gamma$ , $\pi^0$ and $\pi^-$ in the simulation .....	63
C.5	Simulated energy spectrum of the photon from $\Lambda \rightarrow n\gamma$ decay in the simulation ....	63

## List of Tables

1.1 Total and partial weak decay rates of ${}^5_{\Lambda}\text{He}$ hypernucleus shown in the unit of the decay rate of $\Lambda$ in the free space $\Gamma_{\Lambda}$ .....	6
3.1 Momenta and branching ratios of beta decay electron and those of $\pi^{-}$ and $\pi^0$ from main decay modes for ${}^5_{\Lambda}\text{He}$ .....	20
3.2 The reduction rates of detectors and correlation method ( $\Delta z$ ) for the $\pi^0$ and $\pi^{-}$ background events through the analyses with each detector and the correlation method ( $\Delta z$ ) .....	28
4.1 Expected yield of the ${}^5_{\Lambda}\text{He}$ and its beta decay events estimated by the ${}^5_{\Lambda}\text{He}$ yield measured in the KEK E462 experiment and a GEANT4 simulation .....	49
4.2 Expected yield of the ${}^5_{\Lambda}\text{He}$ and proton events from their nonmesonic weak decay and the expected lifetime accuracy, estimated in comparison with the KEK E462 experiment .....	50

# 1 Introduction

## 1.1 Modification of $\Lambda$ 's beta decay in nuclear matter

Since a nucleon is made of quarks and gluons with meson cloud, it is natural to consider that the properties and structure of nucleon may be modified in a nucleus via the interactions between the quarks in the nucleon and the meson fields spread over the nucleus. The only clear evidence for nucleon modification in nuclear matter is the EMC effect. The EMC effect indicates change of the momentum distribution of quarks in the nucleon in nuclear matter, but the mechanism of the change has not been clarified very well [1]. There are theoretical models which predict nucleon modification in a nucleus, but it is difficult to find which theory is correct because experimental data suggesting the baryon modification is quite limited other than the EMC effect. Since there are many-body effects in a nucleus, it was thought difficult to separate the effect of baryon modification from other effects.

We thought of an idea that baryon modification via the meson field may be clearly detected by using the  $\Lambda$  hypernucleus.  $\Lambda$  is the baryon composed of u, d and s quarks, and it has been used to study the properties of the deeply inner part of the nucleus. This is because a  $\Lambda$  baryon is free from Pauli blocking from nucleons, and it can stay in the 0s orbit in the nucleus. In this motivation, our group is now preparing for an experiment (E63) to measure the magnetic moment of a  $\Lambda$  in a nucleus at J-PARC (Japan Proton Accelerator Research Complex). Another possible probe for baryon modification is to investigate weak decay properties of a  $\Lambda$  in a nucleus. It has been discussed that the size of nucleon may be swelled since the spatial distribution of u and d quark wavefunctions may be spread due to their interaction with the meson field in the nucleus. Here, Figure 1.1 shows a schematic view of a  $\Lambda$  in the free space and in the nucleus. As shown in Figure 1.1, it is expected that the spatial distribution of u and d quarks is spread and that of s quarks is unchanged because the coupling of s quarks with the meson field is much smaller than that of u and d quarks. When the beta decay of  $\Lambda$  takes place in the nucleus, the spatial overlap between the u quark wavefunction and the unchanged s quark wavefunction is expected to decrease. This change of the nucleon structure can be measured as a reduction of the axial charge  $g_A$  and then the beta decay rate of  $\Lambda$  in a nucleus. The measurements for  $g_A/g_V$  of a  $\Lambda$  in the free space was taken place, and gave  $g_A/g_V = -0.718 \pm 0.015$  [2]. However, there is no experimental data on  $\Lambda$ 's beta decay in a nucleus.

As described in Section 1.2, according to a calculation by Quark Meson Coupling model (QMC model), the axial charge is predicted to be reduced by 10 % at maximum, and thus the beta decay rates of  $\Lambda$  is predicted to be reduced by 20% at maximum in a nucleus [3].

If the modification of the baryon structure in a nucleus is clearly measured, we will be able to understand how and why the hierarchical structure between the baryon and the quark is separated. In addition, the baryon modification may give a clue to solve the problem of “Hyperon puzzle” for the neutron star mass. If the baryon modification takes place in nuclear matter, the effect of modification should be considered in the neutron star mass calculation. The study of the baryon modification is quite important to develop nuclear physics based on QCD.

This thesis describes our study on how to measure  $\Lambda$ 's beta decay rates.

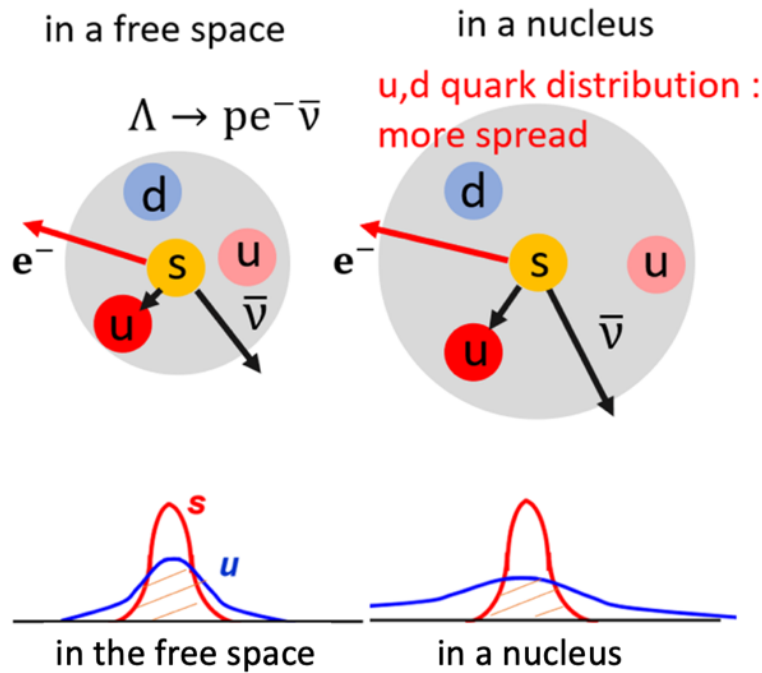


Figure 1.1: Schematic view of the beta decay of a  $\Lambda$  baryon in the free space (left) and in a nucleus (right). When the beta decay takes place, an s quark in the  $\Lambda$  changes to a u quark. In the nucleus, the spatial distribution of u and d quark wavefunctions may be spread due to the meson field, and that of s quarks is unchanged. The overlap of the u and s quarks are expected to reduce, and this change of the baryon structure can be measured via the beta decay rate.

## 1.2 Change of $g_A$ by QMC model

Quark Meson Coupling Model (QMC model) [3] was developed by P. A. M Guichon and A. W. Thomas to describe nuclear properties based on the MIT bag model. QMC model predicts modification of the bound baryon structure via the interactions between u, d quarks in a baryon and mesons in a nucleus. QMC model considers the couplings of the  $\sigma$ ,  $\omega$  and  $\rho$  mesons to the u and d quarks in the baryon, but not to the s quarks. Due to the coupling with the meson field, the effective mass of quarks in the nucleus is changed, and it makes the axial vector charge changed.

Figure 1.2 shows the relation between the change of the axial vector charge  $g_A$  and the nuclear density. Three lines correspond to the different coupling constants of the interaction between quarks and the meson field estimated by three different theoretical methods. As shown in Figure 1.2, the  $g_A$  value decreases for larger densities. Since the saturation density of nucleus is  $0.17 \text{ cm}^{-3}$ , the reduction rate of  $g_A$  is expected to be about  $9 \pm 1.6\%$ .

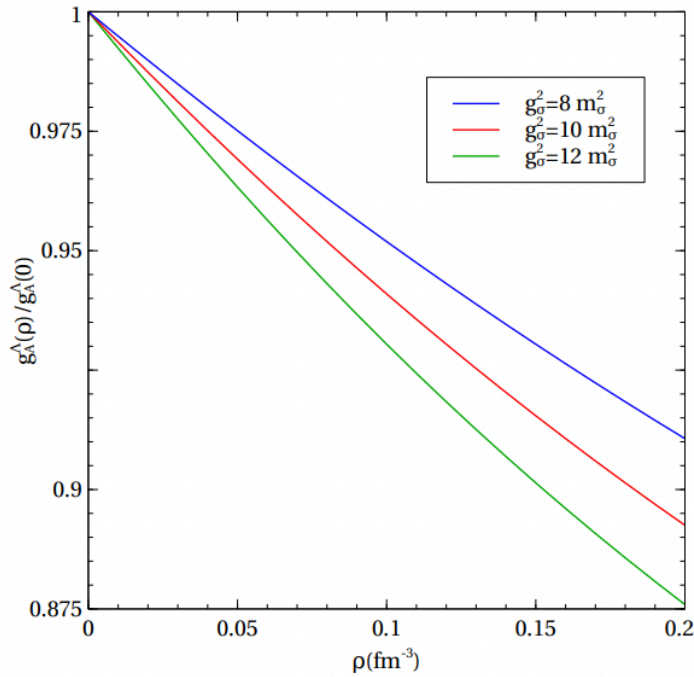


Figure 1.2: Change of the axial vector charge  $g_A$  of a  $\Lambda$  in nuclear density  $\rho$  predicted by QMC model. In the nuclear matter density  $\sim 0.17 \text{ fm}^{-3}$ , the reduction rate is  $9 \pm 1.6\%$  [3].

In general, the beta decay rate,  $\Gamma_{beta}$ , is written in terms of the vector charge  $g_V$ , the axial vector charge  $g_A$ , and nuclear matrix elements as

$$\Gamma_{beta} \propto g_V^2 M_F^2 + g_A^2 M_{GT}^2,$$

as described in Appendix A. This relation is also valid for  $\Lambda$ 's beta decay in a hypernucleus.  $M_F^2$  and  $M_{GT}^2$  are the matrix elements of Fermi transition and Gamov-Teller transition. Here, we consider that  $M_F^2$  and  $M_{GT}^2$  values are the same as those of a  $\Lambda$  in the free space. Then the beta decay rate is given by

$$\Gamma_{beta} \propto g_V^2 + 3g_A^2.$$

When  $\Lambda$ 's beta decay in a nucleus occurs only via Gamov-Teller transition as

$$\Gamma_{beta} \propto 3g_A^2,$$

the beta decay rate decreases by about 20%. When  $\Lambda$ 's beta decay in a  $0^+$  nucleus occurs in combinations of Fermi and Gamov-Teller transition,

$$\Gamma_{beta} \propto g_V^2 + 3g_A^2,$$

the beta decay rate decreases by about 12%.

### 1.3 $\Lambda$ 's weak decay

Figure 1.3 shows the decay branching ratios of a  $\Lambda$  in the free space [2]. As shown in Figure 1.3, the  $\Lambda$ 's main decay modes are mesonic weak decay of  $\Lambda \rightarrow n\pi^0$  and  $\Lambda \rightarrow p\pi^-$ . The branching ratio of the beta decay is  $\sim 8.0 \times 10^{-4}$ , and it is much smaller than that of mesonic weak decay (0.997).

$\Lambda$ DECAY MODES	Fraction ( $\Gamma_i/\Gamma$ )	Confidence level	$p$ (MeV/c)
$p\pi^-$	(63.9 $\pm$ 0.5 ) %		101
$n\pi^0$	(35.8 $\pm$ 0.5 ) %		104
$n\gamma$	( 1.75 $\pm$ 0.15) $\times 10^{-3}$		162
$p\pi^- \gamma$	( 8.4 $\pm$ 1.4 ) $\times 10^{-4}$		101
$p e^- \bar{\nu}_e$	( 8.32 $\pm$ 0.14) $\times 10^{-4}$		163
$p \mu^- \bar{\nu}_\mu$	( 1.57 $\pm$ 0.35) $\times 10^{-4}$		131

Figure 1.3: Decay branching ratios of a  $\Lambda$  in the free space [2].

Table 1.1 shows total and partial weak decay rates of  ${}^5_\Lambda\text{He}$  hypernucleus shown in the unit of the decay rate of  $\Lambda$  in the free space.  $\Gamma_{\pi^-}$ ,  $\Gamma_{\pi^0}$  and  $\Gamma_{\text{nm}}$  are decay widths of mesonic weak decay and nonmesonic weak decay, respectively.  $\Gamma_\Lambda$  and  $\Gamma_{\text{tot}}$  are the sum of the decay widths in the free space and in  ${}^5_\Lambda\text{He}$ , respectively. As shown in Table 1.1, the  $\Lambda$ 's main decay modes are greatly suppressed in the nucleus in comparison with in the free space. This is because the momentum of a proton from  $\Lambda$ 's mesonic decay of  $\sim 100$  MeV/c is smaller than the fermi momentum of  $\sim 260$  MeV/c, and this decay mode is Pauli-blocked. Since the mesonic decay width in  ${}^5_\Lambda\text{He}$  is  $\Gamma_{\pi^-} + \Gamma_{\pi^0} \sim 0.54$ , we estimate the effect from Pauli blocking to be  $\sim 0.6$ . In addition, we can assume that  $\Lambda$ 's beta decay in  ${}^5_\Lambda\text{He}$  is also suppressed by a factor of  $\sim 0.6$ , because the proton momentum after the  $\Lambda$ 's beta decay (0 – 160 MeV/c) and the nucleon momenta after the  $\Lambda$ 's mesonic weak decay ( $\sim 100$  MeV/c) are similar. Therefore, we estimate that the branching ratio of the beta decay in  ${}^5_\Lambda\text{He}$  is  $8.0 \times 10^{-4} \times 0.6 = 0.00048$ .

The momentum of  $\pi^0$  and  $\pi^-$  from  ${}^5_\Lambda\text{He}$  decay was theoretically calculated by Motoba as shown in Figure 1.4 (a), (b) [12]. In the case of  $\pi^0$ , the momentum distribution has a peak at 105.4 MeV/c and maximum momentum is 106.1 MeV/c. In the case of  $\pi^-$ , the momentum distribution has a peak at 100 MeV/c and maximum momentum is 102.4 MeV/c. Figure 1.5 shows the total energy of the neutron-proton pair and the neutron-neutron pair from  ${}^5_\Lambda\text{He}$  nonmesonic weak decay ( $\Lambda p \rightarrow np$  and  $\Lambda n \rightarrow nn$ ) measured in the

Table 1.1: Total and partial weak decay rates of  ${}^5_{\Lambda}\text{He}$  hypernucleus shown in the unit of the decay rate of  $\Lambda$  in the free space  $\Gamma_{\Lambda}$ .

Experiment/Theory	$\Gamma_{tot}/\Gamma_{\Lambda}$	$\Gamma_{\pi^-}/\Gamma_{\Lambda}$	$\Gamma_{\pi^0}/\Gamma_{\Lambda}$	$\Gamma_{nm}/\Gamma_{\Lambda}$
Exp. ( $K^-, \pi^-$ ), BNL [4]	$1.03 \pm 0.08$	$0.44 \pm 0.11$	$0.18 \pm 0.20$	$0.41 \pm 0.14$
Exp. ( $\pi^+, K^+$ ), KEK [5][6]	$0.947 \pm 0.038$	$0.340 \pm 0.016$	$0.201 \pm 0.011$	$0.406 \pm 0.020$
Theor. [7] (YNG)		0.393	0.215	
Theor. [8]		0.386	0.196	
Theor. [9]	0.966			0.358
Theor. [10] (NSC97f)			0.317	
Theor. [11]			0.43	

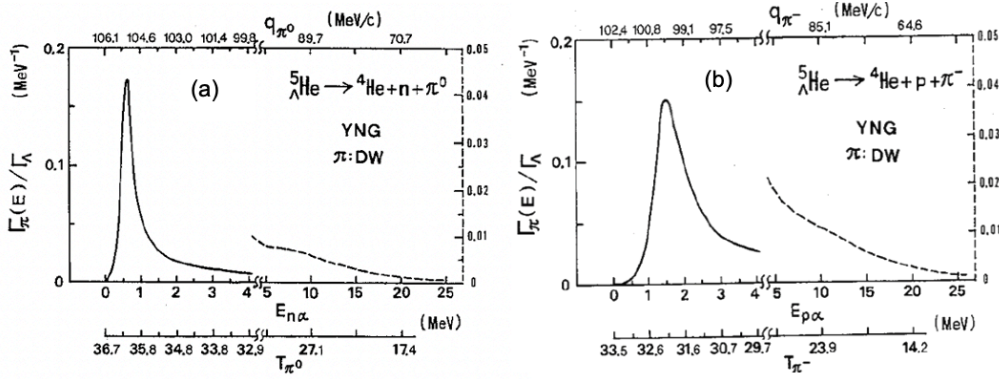


Figure 1.4 (a), (b): Kinetic energy spectra of  $\pi^-$  and  $\pi^0$  (MeV) from  ${}^5_{\Lambda}\text{He}$  calculated by Motoba [12].  $\pi^0$  momentum distribution has a peak at 105.4 MeV/c and maximum momentum is 106.1 MeV/c.  $\pi^-$  momentum distribution has a peak at 100 MeV/c and maximum momentum is 102.4 MeV/c.

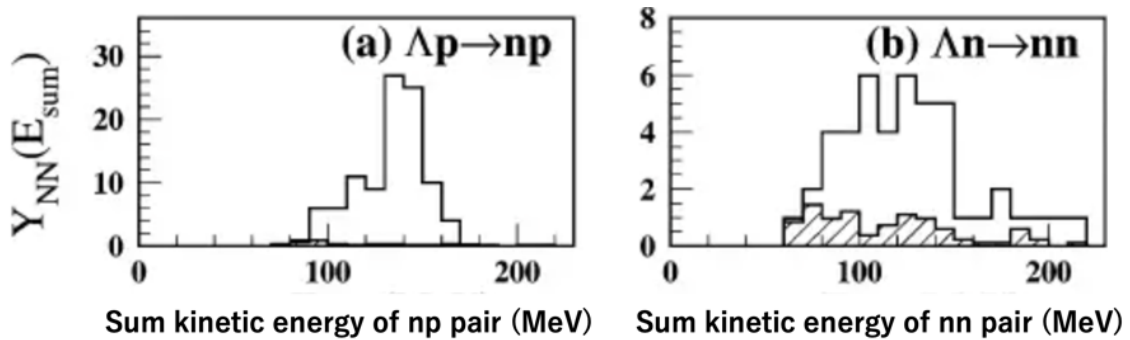


Figure 1.5 (a), (b): The total energy of neutron-proton pair and neutron-neutron pair from  ${}^5_{\Lambda}\text{He}$  weak decay measured in the KEK E462 experiment [13].

KEK E462 experiment [13]. The sum energy distributes in the range of 60 – 220 MeV, and the momentum of nucleon is calculated to be  $< 470$  MeV/c. Energy widely distributes because of Fermi motion.

In addition, we calculate the electron kinetic energy from  $\Lambda \rightarrow pe^- \bar{\nu}_e$ , and the energy distribution distributes in 0 – 163 MeV as shown in Figure 1.6.

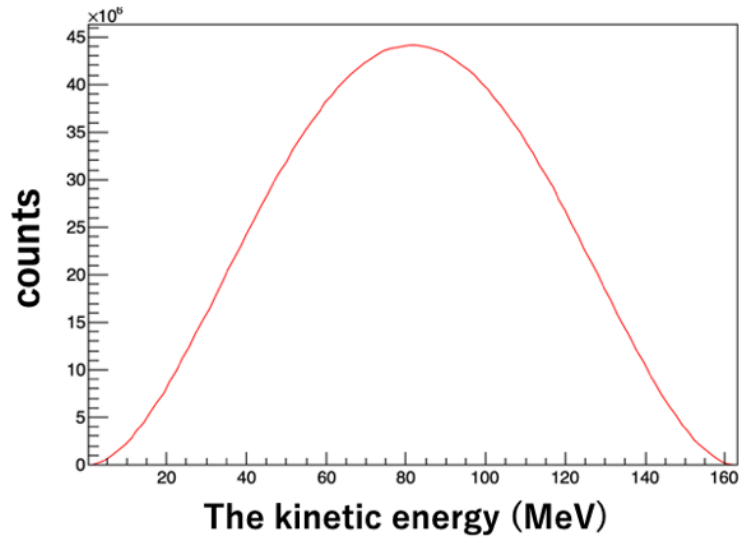


Figure 1.6: The kinetic energy spectra of the beta decay electron from  $\Lambda \rightarrow pe^- \bar{\nu}_e$  decay. The kinetic energy distributes in 0 – 163 MeV.

## 2 Experiment for measuring the $\Lambda$ 's beta-decay rate

### 2.1 Modification of $\Lambda$ in ${}^5_{\Lambda}\text{He}$

According to the calculation of the QMC model, the axial charge  $g_A$  of  $\Lambda$  in nuclear matter density may decrease by 10% at maximum. We want to measure  $g_A$  reduction by separating other effects from baryon modification, but it seems difficult. In the beta decay of ordinary nuclei, nuclear many-body effects and hadronic effects such as meson exchange current are known to reduce the beta decay rate of Gamov-Teller transition. Such reduction is ascribed to quenching of the effective  $g_A$  value in nuclei [14]. Figure 2.1 shows the quenching effects of  $g_A$  in light nuclei [15]. The quenching effects become larger in heavier nuclei.

Reaction	$2J_k^{\pi}, 2T$ (i) (f)	$\log f_{At}$	$M(\text{GT})$ (exp)	$M(\text{GT})$ th(free)	$\frac{M(\text{GT})_{\text{exp}}}{M(\text{GT})_{\text{th(free)}}$
${}^1_0(\beta^-){}^1_0\text{H}$	$1^+, 1 \quad 1^+, 1$	3.024(1)	3.100(7)	3.096	<b>1.00</b>
${}^3_0(\beta^-){}^3_0\text{He}$	$1^+, 1 \quad 1^+, 1$	3.058(1)	2.929(5)	3.096	<b>0.946</b>
${}^6_0(\beta^-){}^6_0\text{Li}$	$0^+, 2 \quad 2^+, 0$	2.910(1)	2.748(4)	3.031	<b>0.907</b>
${}^7_0\text{Be}(\text{EC}){}^7_0\text{Li}$	$3^-, 1 \quad 3^-, 1$	3.300(1)	2.882(4)	3.187	<b>0.904</b>
${}^{11}_0\text{C}(\beta^+){}^{11}_0\text{B}$	$3^-, 1 \quad 3^-, 1$	3.598(2)	1.480(9)	2.084	<b>0.710</b>
${}^{13}_0\text{N}(\beta^+){}^{13}_0\text{C}$	$1^-, 1 \quad 1^-, 1$	3.671(2)	0.788(8)	0.891	<b>0.884</b>

Figure 2.1: The quenching effect of the axial vector charge  $g_A$  for beta decay of various light nuclei. The reduction of  $g_A$  becomes larger for heavier nuclei, but that of the s-shell nuclei is around  $\sim 5\%$  [14,15].

As shown in Figure 2.1, the quenching effect become larger for the heavier nuclei. However, we can see that the quenching effect is small ( $\sim 5\%$ ) for the s-shell ( $A \leq 4$ ) nuclei. Thus, the quenching effect is expected to be about 5% for  ${}^5_{\Lambda}\text{He}$  hypernucleus. For this reason, we propose an experiment to measure the beta decay rate of  ${}^5_{\Lambda}\text{He}$ .

The beta decay rate  $\Gamma_{\text{beta}}$  is described by the branching ratio of the beta decay  $\text{BR}_{\text{beta}}$  and the lifetime of  $\tau_{\Lambda}$  in  ${}^5_{\Lambda}\text{He}$  as  $\Gamma_{\text{beta}} = \text{BR}_{\text{beta}}/\tau_{\Lambda}$ .  $\text{BR}_{\text{beta}}$  is obtained from the number of beta decay events from produced  ${}^5_{\Lambda}\text{He}$  hypernuclei. Considering the available beamtime at J-PARC, we expect that  $\text{BR}_{\text{beta}}$  can be measured within 4% accuracy and  $\tau_{\Lambda}$  can be measured within 2% accuracy. In our proposed experiment, we hope to confirm the reduction of  $\Gamma_{\text{beta}}$  ( $\sim 20\%$  at maximum) with more than  $3\sigma$  confidence level. This goal will be achieved by measuring  $\text{BR}_{\text{beta}}$ ,  $\tau_{\Lambda}$  within 4% and 2% accuracy, respectively. In the case of the  ${}^5_{\Lambda}\text{He}$  lifetime, it was previously measured with 4% accuracy in the KEK E462 experiment [5,6,13]. We will use a similar setup as the KEK E462 experiment and

achieve 2% accuracy, as described later. In the case of the branching ratio, no measurement has been carried out yet.

## 2.2 Production of ${}^5_{\Lambda}\text{He}$ at J-PARC K1.1 beamline

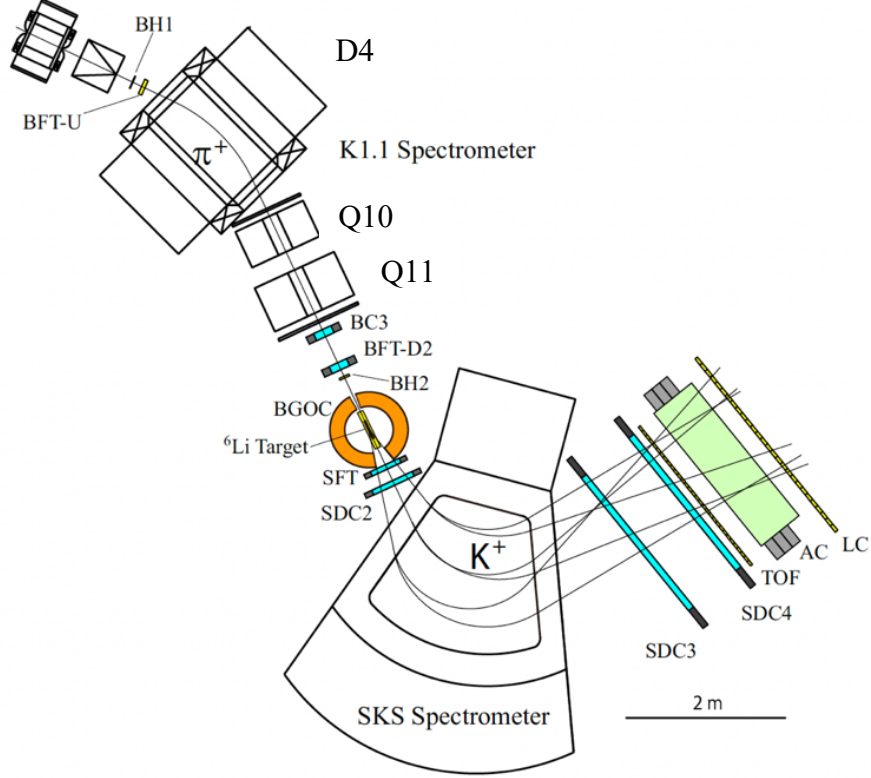


Figure 2.2: Experimental setup for measuring the beta decay rate at J-PARC K1.1 beamline. 1.1 GeV/c  $\pi^+$  beams are provided to the target, and the scattered  $K^+$ 's are identified by the SKS spectrometer.

We plan to carry out measurements of the beta decay rate at the J-PARC K1.1 beamline because the K1.1 beamline is suitable for producing  $S = -1$  hypernuclei. The K1.1 beamline is the secondary beamline which maximumly provides  $\pi^+$  beam with momenta up to 1.1 GeV/c (see the detailed information in Appendix B).

Figure 2.2 shows the experimental setup planned at the K1.1 beamline. The  ${}^5_{\Lambda}\text{He}$  hypernucleus will be produced via the  ${}^6\text{Li}(\pi^+, K^+){}^6_{\Lambda}\text{Li}$  reaction with a  ${}^6\text{Li}$  target. The produced  ${}^6_{\Lambda}\text{Li}$  hypernucleus is unbound and immediately decays as  ${}^6_{\Lambda}\text{Li} \rightarrow {}^5_{\Lambda}\text{He} + p$ , and then the  ${}^5_{\Lambda}\text{He}$  hypernucleus is produced. The production of  ${}^5_{\Lambda}\text{He}$  is identified by the missing mass method. The missing mass is calculated as

$$M_{HYP} = \sqrt{(E_{\pi} + M - E_k)^2 - (\vec{P}_{\pi} - \vec{P}_k)^2}.$$

Here,  $E_\pi, E_K$  are the total energies of the beam  $\pi^+$  and the scattered  $K^+$ , respectively.  $\vec{P}_\pi, \vec{P}_K$  are the momentum vectors of the beam  $\pi^+$  and the scattered  $K^+$ , respectively.  $M$  is the mass of the target nucleus,  ${}^6\text{Li}$ . The momentum of beam  $\pi^+$  is measured by the K1.1 beamline spectrometer, and that of the scattered  $K^+$  is measured by the SKS spectrometer. Figure 2.3 shows the excitation energy spectrum of  ${}^6_\Lambda\text{Li}$  by the  $(\pi^+, K^+)$  reaction [16]. (b) and (c) show the spectra in coincidence with pions and protons. The ground state of  ${}^6_\Lambda\text{Li}$  is clearly seen.

### 2.2.1 Via the $(\pi^+, K^+)$ or $(K^-, \pi^-)$ reaction?

${}^5_\Lambda\text{He}$  can be produced by the  $(\pi^+, K^+)$  or the  $(K^-, \pi^-)$  reactions. Figure 2.4 shows the excitation energy spectrum of the  $(K^-, \pi^-)$  reaction obtained by an old experiment [17]. As shown in Figure 2.4, the ground state of  ${}^6_\Lambda\text{Li}$  is clearly seen, but there are peaks of the unbound states at about 8 MeV and 18 MeV. These states correspond to the orbital angular momentum transfer  $\Delta L = 0$ , and are called “substitutional state”. The substitutional state is likely to be produced in small momentum transfer reactions such as  $(K^-, \pi^-)$  reaction ( $q < 150$  MeV/c with 0.8–1.1 GeV/c beam momentum and  $0^\circ - 10^\circ$  scattering angle). By using large momentum transfer reactions such as  $(\pi^+, K^+)$  reaction ( $q \sim 300$  MeV/c), a large orbital angular momentum transfer  $\Delta L \geq 2$  is given to the hypernucleus, and production of substitutional states are greatly suppressed. According to the KEK E419 experiment in which the  ${}^6_\Lambda\text{Li}$  hypernucleus is produced, the mass resolution was 4.2 MeV using a 13.7 g/cm<sup>3</sup>-thick  ${}^7\text{Li}$  target [18]. In our proposed experiment, we will use almost the same thickness of  ${}^6\text{Li}$  target considering the yield of  ${}^5_\Lambda\text{He}$  (described later). In the case of the  $(K^-, \pi^-)$  reaction, with the mass resolution of  $\sim 4$  MeV, about 10% of the excited substitutional state at 8 MeV contaminates the ground state peak. In the case of the  $(\pi^+, K^+)$  reaction, the substitutional states are not populated. In addition, in the case of  $(K^-, \pi^-)$  reaction,  $\pi^-$  from the beam  $K^-$  decay causes misidentification as  $(K^-, \pi^-)$  reaction. Therefore, we decided to use the  $(\pi^+, K^+)$  reaction for the  ${}^5_\Lambda\text{He}$  hypernucleus production.

### 2.2.2 K1.1 beamline spectrometer

The K1.1 beamline spectrometer is composed of D4, Q10 and Q11 magnets. At the entrance of D4 magnet, a scintillating fiber detector, BFT-U, is installed. At the exit of the beamline, a drift chamber, BC3, and a fiber detector, BFT-D2, are installed. The beam track is reconstructed by three hit points on BC3, BFT-U and BFT-D2. In addition, plastic counter hodoscopes, BH1 and BH2, are installed at the entrance of D4 and the exit of the beamline, respectively. Time-of-flight (TOF) of a particle is measured by flight time from

BH1 to BH2. A beam  $\pi^+$  can be distinguished from other particles and the momentum of  $\pi^+$  is measured. The momentum resolution is expected to be 0.042 % (FWHM) [19].

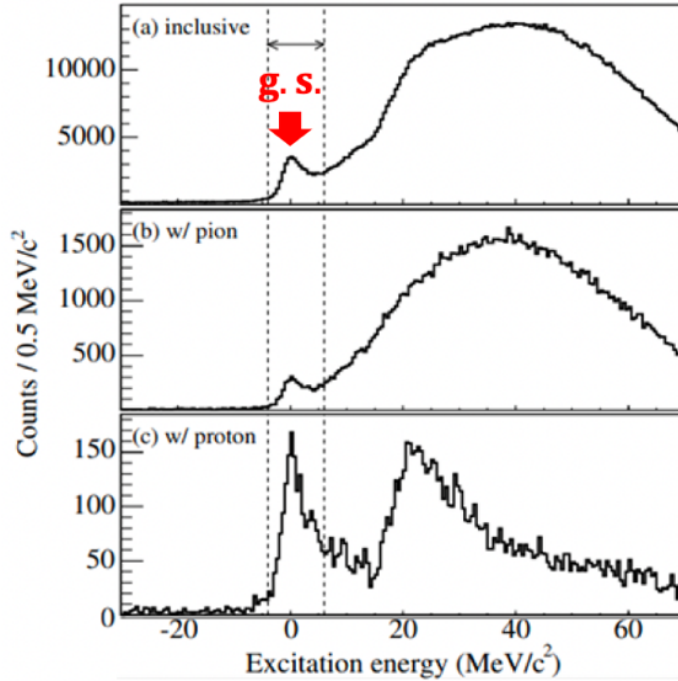


Figure 2.3: The excitation energy spectrum of  ${}^6_{\Lambda}\text{Li}$  by the  $(\pi^+, K^+)$  reaction measured in the KEK E462 experiment [16]. (b) and (c) show the spectra in coincidence with pions and protons. The ground state of  ${}^6_{\Lambda}\text{Li}$  is clearly seen in any of the coincidence spectra.

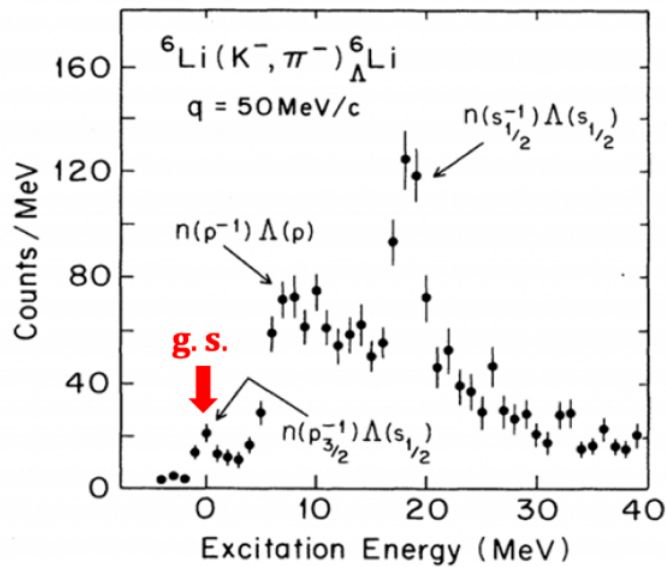


Figure 2.4: The excitation energy spectrum of the  ${}^6_{\Lambda}\text{Li}$  by the  $(K^-, \pi^-)$  reaction. The ground state of  ${}^6_{\Lambda}\text{Li}$  is clearly seen, but substitutional states at 8 MeV and 18 MeV excitation are more prominent [17].

### 2.2.3 SKS spectrometer

The SKS spectrometer is composed of a superconducting dipole magnet (SKS magnet), three drift chambers (SDC2, SDC3, SDC4), time of flight detectors (TOF) and aerogel Cerenkov counters (AC). TOF identifies  $K^+$  by using flight time from BH2 to TOF. AC separates scattered  $K^+$  from beam  $\pi^+$ . SDC2-4 record scattered particle tracks. Via these devices, a scattered  $K^+$  can be distinguished from other particles and the momentum of  $K^+$  is measured. The SKS covers a wide range of scattering angle ( $-15^\circ \sim 15^\circ$ ), which is larger than the angular range ( $-10^\circ \sim 10^\circ$ ) of the scattered  $K^+$  in the  $(\pi^+, K^+)$  reaction. The momentum acceptance of the SKS spectrometer is  $0.7 - 1.1$  GeV/c, and the acceptance of SKS is about 100 msr.

### 2.2.4 ${}^6\text{Li}$ target

To achieve  $\sim 4$  MeV mass resolution of hypernucleus and clearly see the ground state peak of  ${}^6_\Lambda\text{Li}$  in  $(\pi^+, K^+)$  reaction, we will use a 90% enriched  $14 \text{ g/cm}^3$   ${}^6\text{Li}$  target with a cylindrical shape. We expect that a length of  ${}^6\text{Li}$  target is 30cm and diameter is 3 cm to cover diameter of beam  $\pi^+$ . The target is packed in a laminated plastic bag filled with Ar gas.

## 2.3 Apparatus around the target for measuring the branching ratio of the beta decay

After the production of  ${}^5_{\Lambda}\text{He}$ , the beta decay electron from the hypernucleus should be measured. We want to measure the beta decay electron as many as possible by the detectors surrounding the Li target. When measuring the beta decay electron, there is a problem of the background from  $\Lambda$ 's other decay modes. As shown in Table 1.1, the expected background is as follows.

- Mesonic weak decay  $\Lambda \rightarrow p\pi^-, \pi^- pn \rightarrow nn$  (BR = 0.4)
- Mesonic weak decay  $\Lambda \rightarrow n\pi^0, \pi^0 \rightarrow \gamma\gamma$  (BR = 0.2)
- Nonmesonic weak decay  $\Lambda n \rightarrow nn$  and  $\Lambda p \rightarrow np$  (BR = 0.4)

We must distinguish the beta decay electron from the other particles such as  $\pi^-, p, \gamma$  and  $n$ . The beta decay electron is a charged particle with a velocity  $\beta \sim 1$ . The background can be rejected by using this character. We made a rough design of the detectors around the Li target as shown in the followings.

The detectors are composed of

1. Plastic counters  
to separate charged particles and noncharged particles,
2. Lucite Cerenkov counters (index  $n = 1.5$ )  
to detect charged particle with  $\beta > 0.67$ , and
3. BGO calorimeter  
to measure the energy of the beta decay electron.

The geometry of each detector is shown in Figure 2.5. The Li target is surrounded by the plastic counters and the lucite Cerenkov counters, and then the BGO calorimeter. As shown in Figure 2.5, the beta decay electron from  ${}^5_{\Lambda}\text{He}$  hypernucleus produced via the  $(\pi^+, K^+)$  reaction is emitted from the Li target. The beta decay electron is identified by the plastic counters and the lucite Cerenkov counters, and then the energy is measured in the BGO calorimeter. We expect that the number of the beta decay electrons is counted in the final energy spectrum in the BGO. The detailed information of each detector is shown in the next sections.

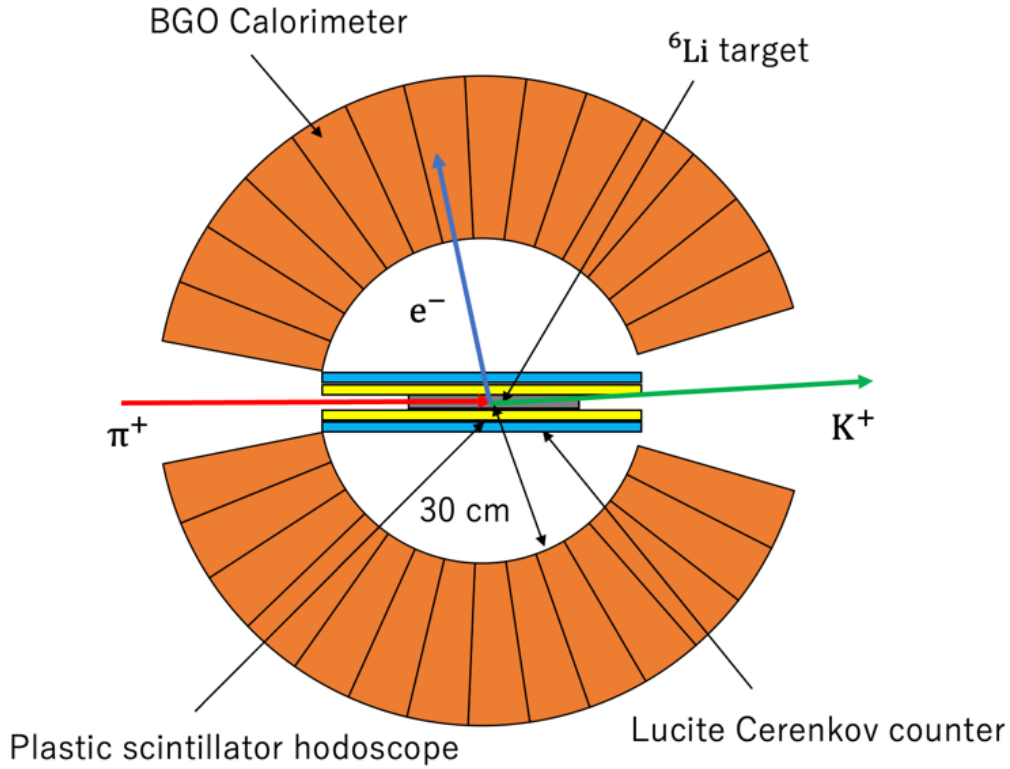


Figure 2.5: Schematic view of the setup for measuring the branching ratio. A  ${}^6\text{Li}$  target is surrounded by plastic counters, lucite Cerenkov counters and a BGO calorimeter. The BGO calorimeter has two holes at upstream and downstream for the beam and the scattered  $K^+$ . The beta decay electron from  ${}^5_\Lambda\text{He}$  is separated from the other particles by the plastic counters and the lucite Cerenkov detectors, and then the energy is measured by the BGO.

## 2.4 Detectors around the Li target

### 2.4.1 BGO calorimeter

The BGO calorimeter measures the total beta decay electron energy which distributes 0 – 163 MeV. The beta decay electron produces an electromagnetic shower in the BGO. The Moliere radius and the depth of the electromagnetic shower are roughly estimated to be  $\sim 2 X_0 = 2.2$  cm and  $\sim 20 X_0 = 22$  cm. Here,  $X_0 \approx 1.1$  cm is the radiation length of BGO. The target is surrounded by spherically shaped segmented BGO counters. We assume the width of BGO crystal is 7 cm and the thickness is 20 cm (7 cm  $\times$  7 cm  $\times$  20 cm crystal) to accept most of the electromagnetic shower from the beta decay electron. The BGO calorimeter is divided by the  $\theta$  and  $\phi$  directions, and the number of the BGO

segments is  $15 (\theta) \times 15 (\phi) = 225$ . These dimensions will be further optimized considering the preparation time and the cost. The signal is read out by a PMT which is attached at the outer end of each BGO crystal.

### 2.4.2 Plastic counter

The Li target is surrounded by the circumferentially segmented plastic counters. Its length is 60 cm (the same as the BGO inner diameter) to detect the beta decay electrons as many as possible. It has a 5 mm thickness and a 6 mm width. By analyzing the energy deposit in the plastic counters, we can measure the velocity of the particles from the energy loss per path length ( $dE/dx$ ). Since the cross section of each plastic scintillator rod is small, we will use MPPCs for reading out a signal. MPPCs are attached at both ends of the plastic and the hit position is measured via the timing difference and the segment number. Namely, the z hit position is obtained from the timing difference and the x, y hit positions are obtained from the segment number with a hit. We expect that the time resolution of the plastic counters and the position resolution along the beam direction to be 100 ps and 20 mm in rms, respectively.

### 2.4.3 Lucite Cerenkov counter

The Li target and the plastic counters are surrounded by circumferentially segmented lucite Cerenkov counters (index  $n = 1.5$ ). Its length is 60 cm (the same as the BGO inner diameter and the length of the plastic counters). It has a 5 mm thickness and a 6 mm width. By using the lucite Cerenkov counter, the beta decay electron can be distinguished from other charged particles such as pions and protons from the hypernucleus decay ( $\beta_{\pi^-} \leq 0.6$  for  $P_{\pi^-} \leq 101$  MeV/c, and  $\beta_p \leq 0.4$  for  $P_p \leq 400$  MeV/c). MPPCs are attached at both ends of each lucite Cerenkov counter. We expect that the efficiency is more than 99% for electrons. According to a GEANT4 simulation (described later), the misidentification rate for the charged pions and protons due to  $\delta$  ray emission in the target is found to be  $\sim 4\%$ .

## 2.5 Setup for measuring the lifetime

Figure 2.6 shows a schematic view of the apparatus for measuring the lifetime of  ${}^5_{\Lambda}\text{He}$  [20]. The experimental setup is similar to that of the KEK E462 experiment. A block of the  ${}^6\text{Li}$  target is surrounded by the timing counter T1 and T2L / T2R. The target in this experiment is different from the target for measuring the branching ratio. It has a 3 cm thickness and a 10 cm length. T1 is made of 20 pieces of 2 mm-wide 50 mm-long 5 mm thick plastic counter, and the signal of each piece is read out by MPPCs attached at both ends. THL and THR are made of 80 pieces 3 mm-thick plastic counters of 2 mm wide and 80 mm long, read out via MPPC's at both ends. T1 measures the timing of the beam pion and T2L or T2R measure the timing of the proton from nonmesonic weak decay of  ${}^5_{\Lambda}\text{He}$ . In addition, THL, THR, T2L and T2R measure the hit position of the proton. BFT-D and T1 also measure the position of the beam pion. The time difference between the T1 hit and the T2L or T2R hit is used to calculate the decay time of hypernuclei after correcting for the pion flight time between T1 and the reaction point, and the proton flight time between T2L or T2R and the reaction point. We will use 2 mm-wide plastic counter to improve the resolution of the hit positions. We expect that the time resolution of T1 and T2L / T2R is better than 50 ps in rms, and the resolution of the hit position is  $\sim 2$  mm. This position resolution corresponds to the resolution of the decay time of  $\sim 10$  ps. T2L and T2R are made of 20 pieces of 4 mm-wide 150 mm-long 5 mm-thick plastic counter, each of which is read out via MPPC's at both ends. Data of the E462 experiment for the difference of timing between the beam  $\pi^+$  and the decay proton at the reaction point in the target is plotted in Figure 2.7 (left for  ${}^5_{\Lambda}\text{He}$  and right for  ${}^{12}_{\Lambda}\text{C}$  data) [16]. This spectrum is called "decay time spectrum". By fitting the decay time spectrum, the lifetime of  ${}^5_{\Lambda}\text{He}$  is obtained. In the E462 experiment, the accuracy for measuring the lifetime is about 4% for  ${}^5_{\Lambda}\text{He}$ . In our proposed experiment, we want to achieve 2 % accuracy for 120 hours (5 day) beamtime (will be described in the chapter 4).

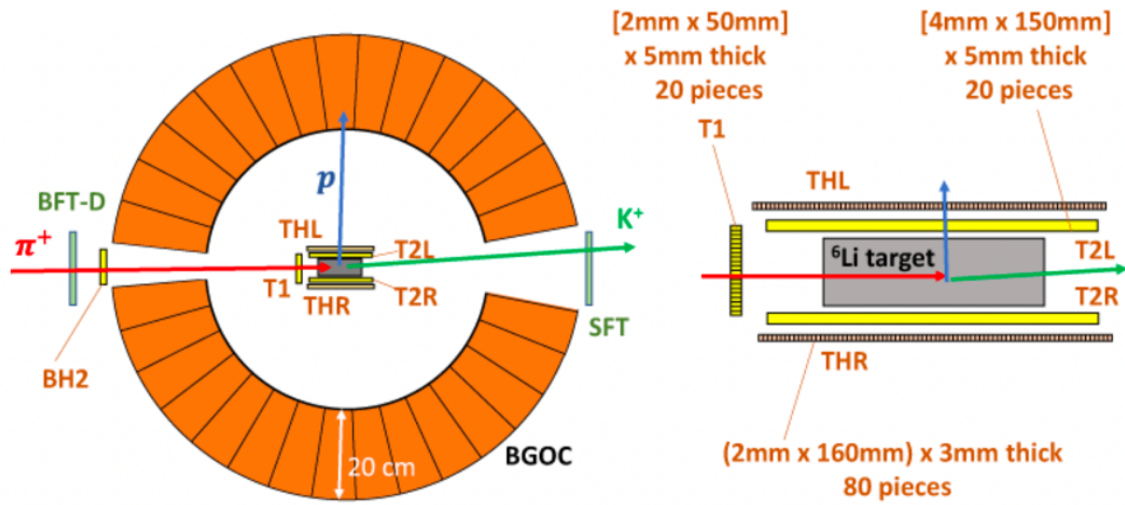


Figure 2.6: A schematic view of the expected set up around the target for the lifetime measurement [20]. The lifetime of a  $\Lambda$  is measured by the timing difference of the timing counters, T1 and T2.

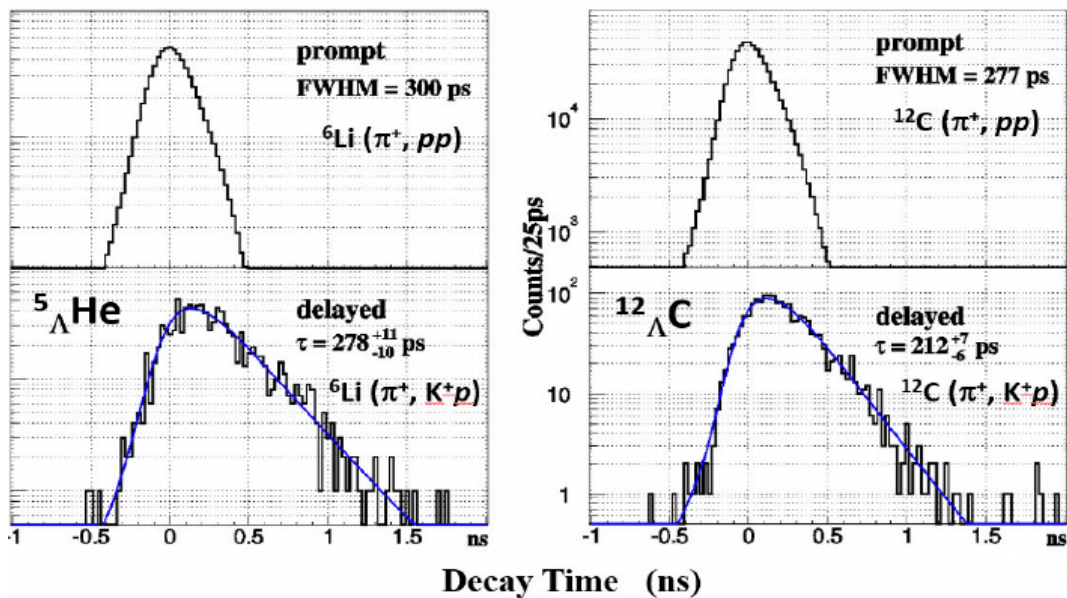


Figure 2.7: The decay time spectra for  ${}^5_{\Lambda}\text{He}$  (left) and  ${}^{12}_{\Lambda}\text{C}$  (right) measured in the KEK E462 experiment [16]. The upper figures show “response function” of the spectrum measured with the prompt reaction of  $(\pi^+, pp)$ . The lower figures show decay time spectra for  ${}^5_{\Lambda}\text{He}$  and  ${}^{12}_{\Lambda}\text{C}$  hypernuclei via the  $(\pi^+, K^+p)$  reaction measured with protons emitted via nonmesonic weak decay of  ${}^5_{\Lambda}\text{He}$ .

### 3 Background reduction study for the branching ratio

To achieve 4.5% accuracy of measuring the beta decay rate of  $\Lambda$ , the background from  $\Lambda$ 's decay modes should be suppressed down to the order of 1% of the beta decay electron signal.

#### 3.1 Principles of background suppression and simulations

In Chapter 2, we discussed the apparatus around the Li target for measuring the beta decay rate of the  ${}^5_\Lambda\text{He}$  hypernucleus and reducing the background from the  $\Lambda$ 's decay. The following detectors are introduced in Chapter 2.

- The BGO calorimeter (225 BGO segments and 7 cm  $\times$  7 cm  $\times$  20 cm crystal)
  - Measure the energy of the beta decay electron.
- The plastic counter (30 segments with 60 cm length, 5 mm thickness and 6 mm width)
  - Identify charged particles (distinguish the beta decay electron from  $\pi^0$ )
- The lucite Cerenkov counter (30 segments with 60 cm length, 5 mm thickness and 6 mm width)
  - Identify charged particles with velocity  $\beta > 0.67$  (distinguish the beta decay electron from  $\pi^-$  and proton from weak decay of  ${}^5_\Lambda\text{He}$ ).

Figure 3.1 shows an illustration of events when the beta decay electron, as well as  $\pi^0$  and  $\pi^-$  from the  $\Lambda$ 's main decay (background), are produced. We expect that the beta decay electron produces one-cluster hit in the BGO calorimeter.  $\pi^0$  mainly decays to  $2\gamma$  ( $\pi^0 \rightarrow 2\gamma$ ), and is expected to produce two-cluster hit in the BGO. When  $\pi^-$  enters the BGO,  $\pi^-$  is expected to interact with the nuclei in BGO by  $\pi^-$  absorption mainly via  $\pi^- \text{ "pn" } \rightarrow \text{nn}$ . Emitted neutrons produce hits in many segments.

In the case of  $\pi^0$ , when one photon from the  $\pi^0 \rightarrow 2\gamma$  decay escapes from the BGO upstream or downstream hole, the other photon produces one-cluster hit in the BGO. Since the solid angle of the upstream or downstream hole is 30.7 msr and 89.8 msr, respectively, the probability of the photon-leak event is  $100 \times (39.8 + 89.8) \times 10^{-3} / 4\pi \approx 1$  (%). In addition, when one photon from  $\pi^0$  converts to  $e^-e^+$ , it is identified as the beta decay electron by the plastic counters. The conversion rate of  $\gamma \rightarrow e^-e^+$  in the plastic and the target is estimated to be about 4% by calculating the cross section of pair creation of photon. Considering the branching ratio of  $\pi^0$  decay of  ${}^5_\Lambda\text{He}$  (0.2) and the branching ratio of the beta decay (0.00048), the estimated background rate per beta decay electron signal is  $0.2 \times 0.01 \times 0.04 \div 0.00048 = 0.16$  (16%).

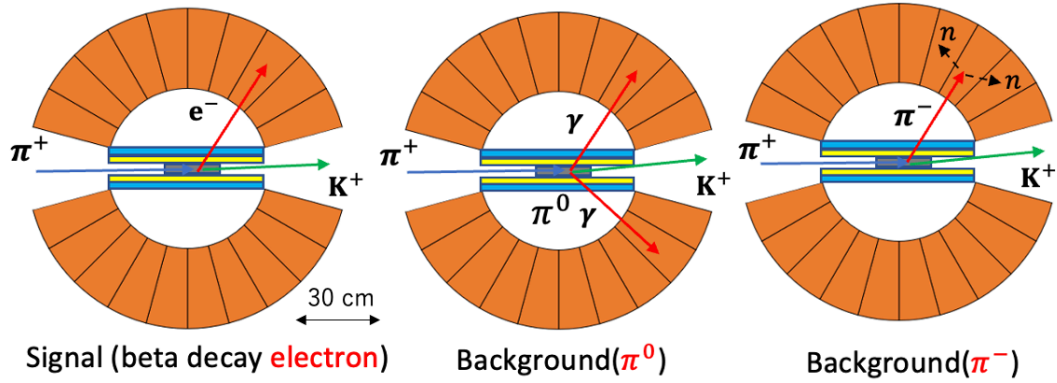


Figure 3.1: An illustration of events of the beta decay electron (signal) as well as  $\pi^0$  and  $\pi^-$  from the  $\Lambda$ 's main decay modes (background). See text for details.

In the case of  $\pi^-$ , the remaining events depend on the misidentification rate by  $\delta$  rays in the lucite Cerenkov counters. Thus, we studied it by a GEANT4 simulation (described later)

Since we need to reduce the background to the order of 1% of the beta decay electron, we have developed various methods of reducing background using GEANT4 simulation code (GEANT4 is a platform developed by CERN for simulating tracks of particles in materials by using Monte Carlo methods).

In Chapter 3, we describe simulations for the  $\Lambda$ 's main decay mode of mesonic weak decay and then non-mesonic weak decay. We also made a simulation for optimization of the BGO detector.

### 3.2 $\pi^0$ and $\pi^-$ background study

Figure 3.2 shows a geometry of setup around the target in GEANT4. The Li target is surrounded by the plastic scintillators (red), the lucite Cerenkov counters (blue) and the BGO calorimeter (cyan). A red plate installed at the BGO downstream hole is a photon veto counter to detect leak photon from  $\pi^0 \rightarrow \gamma\gamma$ . In this simulation, beta decay electron,

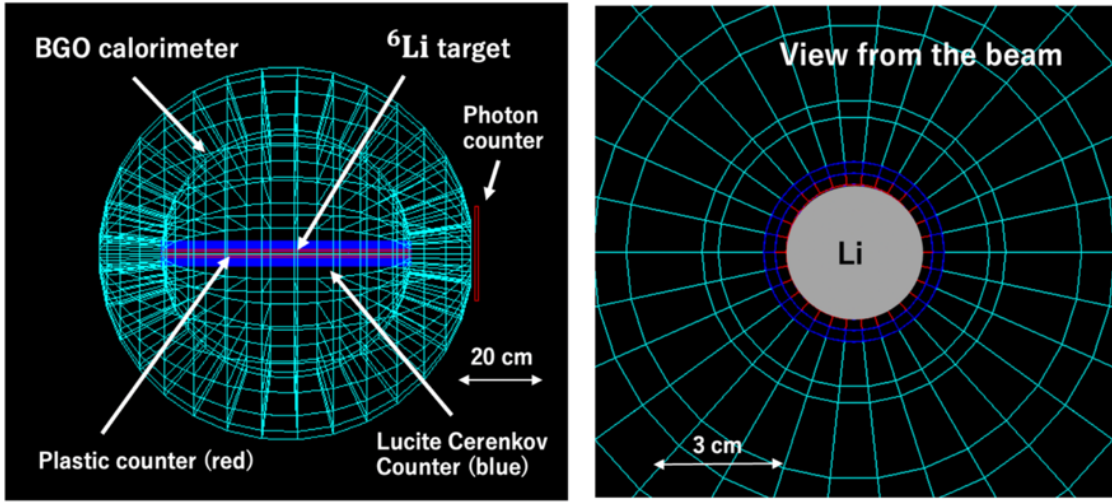


Figure 3.2: Apparatus around the target in the present GEANT4 simulation. The Li target is surrounded by the plastic scintillators (red), lucite Cerenkov counters (blue) and the BGO counters (cyan). Red plate installed at the BGO downstream hole is a photon veto counter.

$\pi^0$  and  $\pi^-$  are produced according to their branching ratios and momenta. The branching ratio of  $\pi^0$  and  $\pi^-$  are taken from the previous experiment (KEK E462) as listed in Table 1.1. Their branching ratios and momenta we used in the GEANT4 simulation are listed in Table 3.1.

Table 3.1: Momenta and branching ratios of beta decay electron and those of  $\pi^-$  and  $\pi^0$  from main decay modes for  ${}^5_{\Lambda}\text{He}$ .

Particle	Beta decay electron	$\pi^0$ ( $\Lambda \rightarrow n\pi^0$ )	$\pi^-$ ( $\Lambda \rightarrow p\pi^-$ )
Momentum (MeV/c)	0 – 163	105.4	100
BR (in ${}^5_{\Lambda}\text{He}$ )	0.00048	0.4	0.2

### 3.2.1 Cluster analysis in BGO counter

Background from  $\pi^0$  and  $\pi^-$  can be greatly rejected via cluster analysis in BGO. Figure 3.3 shows the number of clusters in BGO, and Figure 3.4 shows an example of the BGO hit pattern showing the BGO segments with more than 1 MeV energy loss. A cluster is identified when segments with more than 1 MeV adjoin each other, or a single segment has energy loss over 1 MeV. As shown in Figure 3.4, a beta decay electron produces one-cluster. A  $\pi^0$  mainly produces two-cluster since  $\pi^0$  mainly decays to  $2\gamma$ . In this simulation, Dalitz decay mode  $\pi^0 \rightarrow e^-e^+\gamma$  is also considered, and this mode produces two or three clusters. One cluster of  $\pi^0$  is caused by one  $\gamma$  escape from the BGO upstream or downstream hole. A  $\pi^-$  produces many clusters by many neutrons and nuclear  $\gamma$ -rays from interaction between  $\pi^-$  and nuclei in BGO. It was found that, by selecting one-cluster events as beta decay electron, 97% of  $\pi^0$  and 92.8% of  $\pi^-$  events can be rejected.

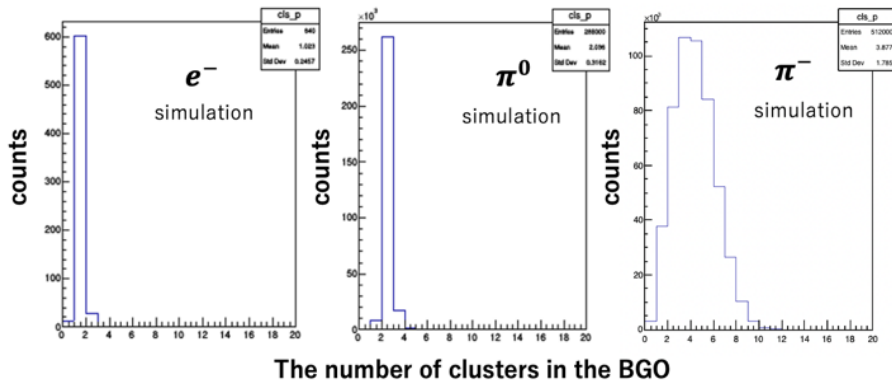


Figure 3.3: The number of clusters in BGO for beta decay electron,  $\pi^0$  and  $\pi^-$  from  ${}^5_{\Lambda}\text{He}$  decay in the simulation. The beta decay electron produces one cluster,  $\pi^0$  produces two clusters by  $\pi^0 \rightarrow \gamma\gamma$ , and  $\pi^-$  produces several clusters due to neutron emission from BGO.

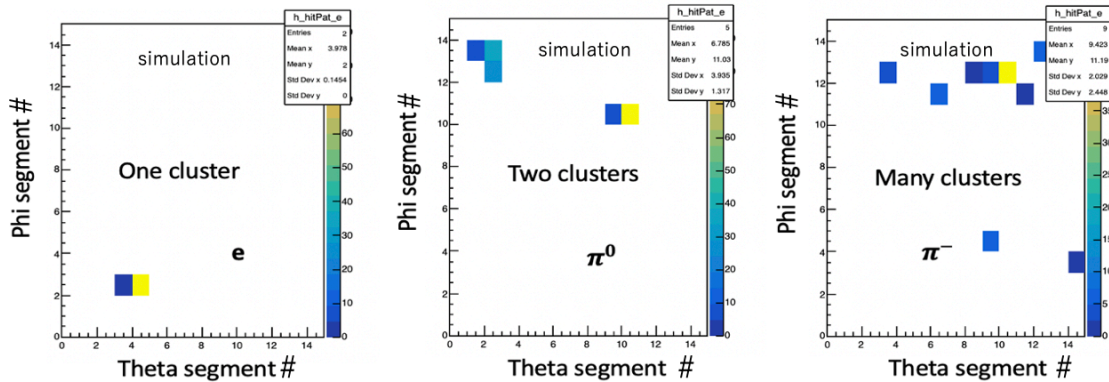


Figure 3.4: Examples of simulated hit patterns in BGO segments for the beta decay electron,  $\pi^0$  and  $\pi^-$  events.

### 3.2.2 Analysis in the plastic counter

Analysis of energy deposit in the plastic counters plays an important role in reducing background. Figure 3.5 shows total energy loss of beta decay electron,  $\pi^0$  and  $\pi^-$  from  ${}^5_\Lambda\text{He}$  decay. As shown in Figure 3.5, the beta decay electron shows a peak of MIP, while the  $\pi^-$  from  $\Lambda$  decay with momenta lower than 100 MeV/c makes a peak at larger energy deposit. The energy loss of  $\pi^0$  widely distributes. The low energy ( $< 1$  MeV) part comes from photoelectric effect and Compton scattering, and the high energy ( $>1$  MeV) part comes from  $e^-e^+$  pair creation. According to the Bethe-Bloch equation, energy loss of electron ( $-dE/dx)_e$  is about  $2 \text{ MeV g}^{-1} \text{ cm}^2$ . We expect that the energy loss per length in plastic is about  $2 \text{ MeV g}^{-1} \text{ cm}^2 \times 0.5 \text{ g cm}^{-3} = 1 \text{ MeV cm}^{-1}$ . To distinguish beta decay electron from  $\pi^0$  using this energy loss spectrum, we calculate energy deposit per path length in the plastic counter.

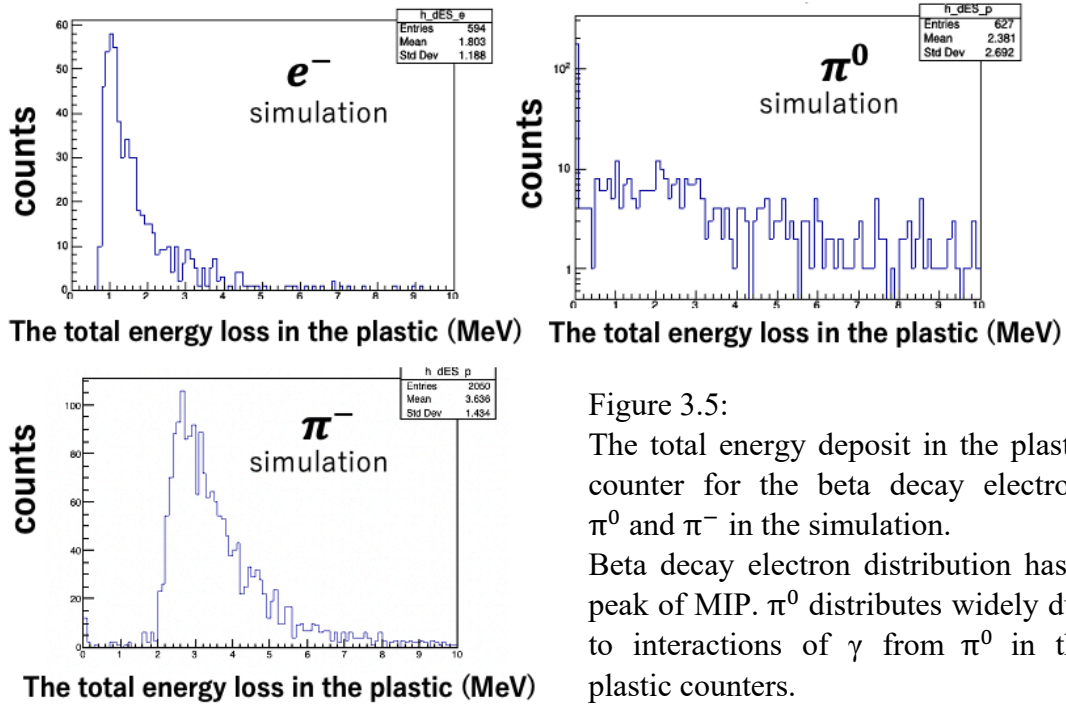


Figure 3.5: The total energy deposit in the plastic counter for the beta decay electron,  $\pi^0$  and  $\pi^-$  in the simulation. Beta decay electron distribution has a peak of MIP.  $\pi^0$  distributes widely due to interactions of  $\gamma$  from  $\pi^0$  in the plastic counters.

Figure 3.6 shows a schematic view of the detectors around the target. Point A, B, C, D are the generation point in the Li target, the position where the particle enters the plastic counter, the position where the particle exits the plastic counter and the hit position of BGO. The point B and C are calculated as the intersections of the line AD and the inner and outer surfaces of the plastic counters, and then the length of BC (path length) is calculated. In this simulation, we assumed the resolution of the generation point A is  $\sigma_x = 1.2 \text{ mm}$ ,  $\sigma_y = 2.6 \text{ mm}$  and  $\sigma_z = 22 \text{ mm}$ . These values were measured in the E13

experiment at J-PARC as the resolution of the vertex point determined from the beam track and the scattered particle track [21]. The E13 experiment was previously carried out at the J-PARC K1.8 beamline, and production events of hypernuclei via the  $(K^-, \pi^-)$  reaction are identified by the beamline spectrometer and the SKS spectrometer. The beta decay experiment will be carried out at the J-PARC K1.1 beamline, but the setup is almost the same as the E13 experiment. Therefore, we used the experimental data of the E13 experiment. Figure 3.7 shows the 2D plot of the path length and the total energy deposit. In the case of the beta decay electron, the total energy deposit of beta decay electron is proportional to the path length due to the constant  $-dE/dx$  from a MIP passing in the plastic counter. In the case of  $\pi^0$ , the total energy deposit has a higher energy component than the energy deposit by a MIP. This is because of multiple charged particles from pair production. We found that the ratio of the total energy deposit to the path length (the energy deposit per path length) can distinguish beta decay electron from  $\pi^0$ . Figure 3.8 shows the energy deposit per path length. The  $\pi^0$  distribution has two peaks corresponding to either of  $e^-$  or  $e^+$ , and to both  $e^-$  and  $e^+$ . By this calculation, separation of  $\pi^0$  and beta decay electron becomes better than comparing of the total energy deposit. After selecting 0.7 – 3.0 MeV as the beta decay electron in the total energy deposit (around a MIP peak), we select 0.12 – 0.25 MeV/mm in the energy deposit per path length as the beta decay electron. Finally, 88% of  $\pi^0$  and 99.9% of  $\pi^-$  events are reduced.

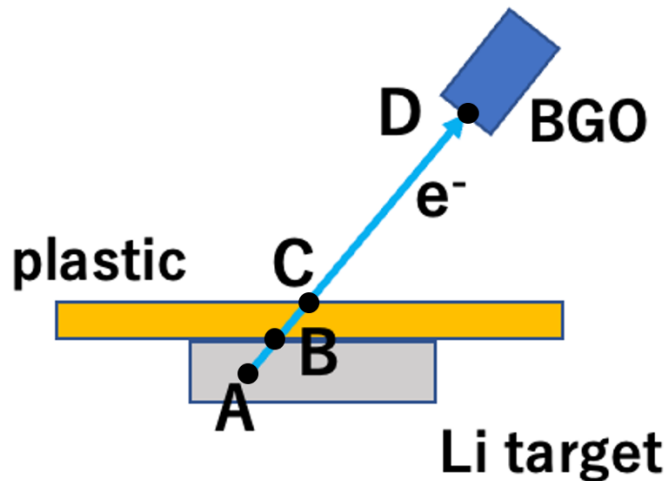


Figure 3.6: Schematic view of the detectors around the Li target. Beta decay electron is produced at A. Then the electron hits the inner and outer surfaces of the plastic counter at B, C and hits BGO at D.

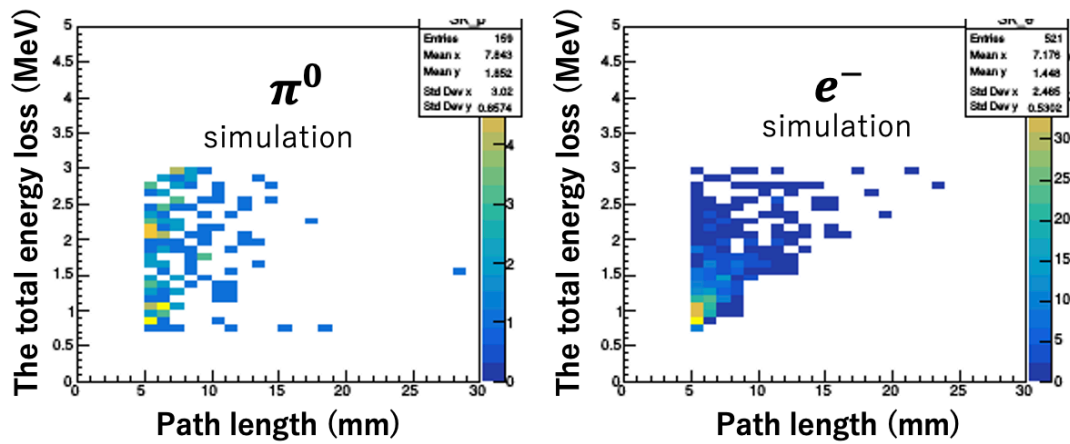


Figure 3.7: Simulated 2D plot of the total energy deposit and the path length in the plastic counter for  $\pi^0$  and the beta decay electron. Left figure shows  $\pi^0$  events and right figure shows the beta decay electron events.

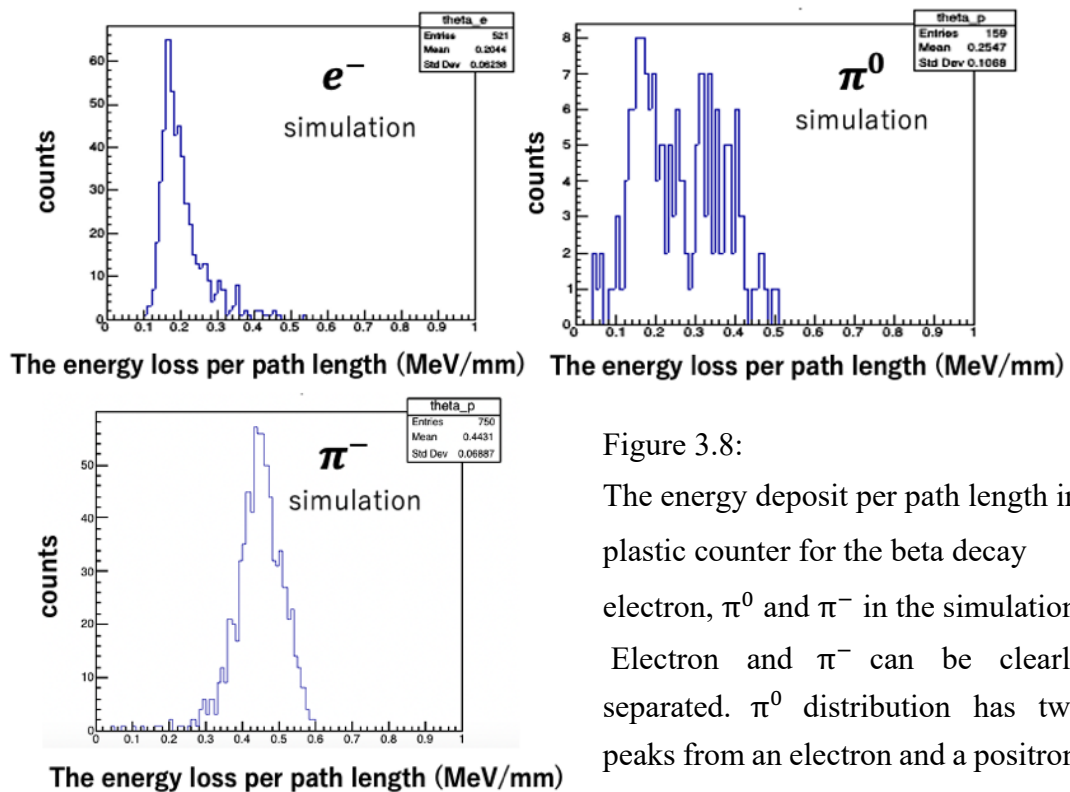


Figure 3.8: The energy deposit per path length in plastic counter for the beta decay electron,  $\pi^0$  and  $\pi^-$  in the simulation. Electron and  $\pi^-$  can be clearly separated.  $\pi^0$  distribution has two peaks from an electron and a positron.

### 3.2.3 Analysis in lucite Cerenkov counter

Since the index of lucite is  $n=1.5$ , lucite Cerenkov counter can distinguish  $\beta > 1/n = 0.67$  from those with  $\beta < 0.67$ . We found that 99.8 % of beta decay electron events can be detected by the lucite Cerenkov counters, and  $\pi^-$  and  $\pi^0$  events are rejected by about 95.5% and 90%, respectively. In addition, 4.5% of  $\pi^-$  events are found to emit  $\delta$  rays and they are misidentified as beta decay electron.

### 3.2.4 Correlation between hit positions of detectors

When one photon from  $\pi^0$  decay escapes from the BGO hole, the other photon may become background for beta decay electron. The other photon produces electromagnetic shower in BGO, and charged particles ( $e^+$  and  $e^-$ ) sometimes escape from BGO. If the escaping charged particles enter the plastic counters and the lucite Cerenkov counters, these particles are misidentified as beta decay electron.

Figure 3.9 shows schematic views of a beta decay electron event and a misidentified event of  $\pi^0$ . Points O, A, B are the generation point, and the hit points in the plastic counter and BGO. Point C is intersection of the line OB and the plastic counter. With respect to the point C, the z position is determined by timing difference of MPPCs attached on both ends of the plastic counter, and x, y positions are determined by the segment number divided in  $\varphi$  direction. Regarding the point B, the hit position is determined by the cluster center in BGO. To calculate the cluster center, energy deposits in hit segments are weighted. Finally, the difference of z position between A and C ( $\Delta z$ ) is calculated. As shown in Figure 3.10, in the case a beta decay electron event,  $\Delta z$  distributes around 0 because a track of beta decay electron is a straight line. In the case of misidentified  $\pi^0$ ,  $\Delta z$  widely distributes since charged particles which are produced from electromagnetic shower in BGO and escape back from BGO hits the plastic counter. By selecting  $-90 \text{ mm} < \Delta z < 90 \text{ mm}$  as beta decay electron, 20 % of  $\pi^0$  events are rejected.

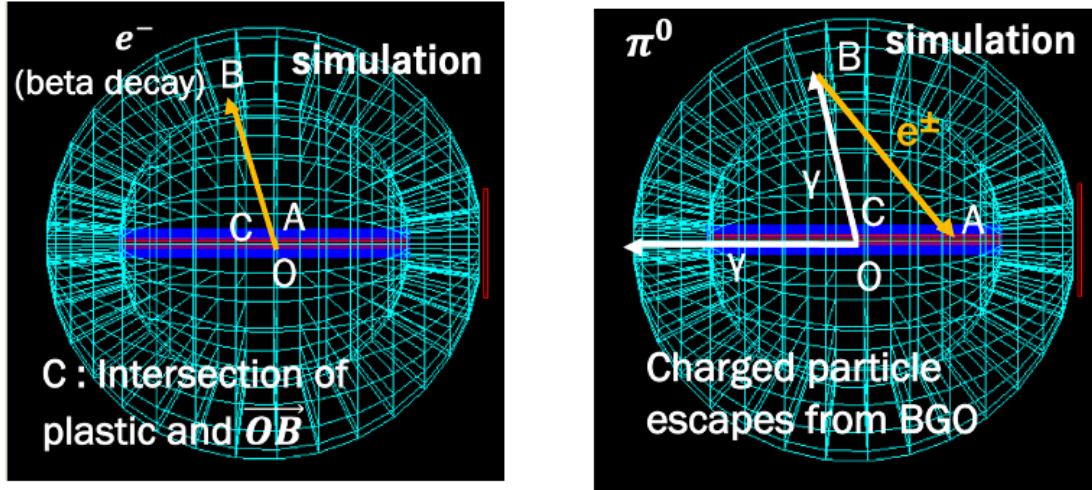
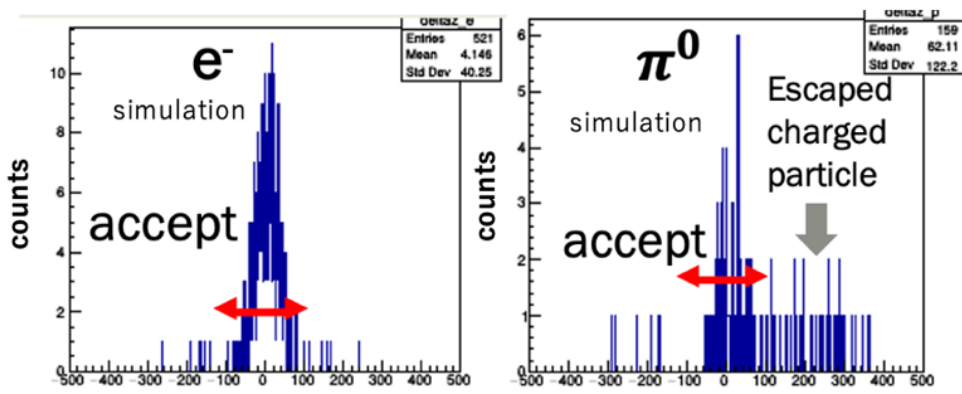


Figure 3.9: Schematic views of a beta decay electron event and a misidentified  $\pi^0$  event in the simulation. Charged particles ( $e^\pm$ ) from the electromagnetic shower produced by the photon from  $\pi^0$  decay hit the plastic counters, and they are misidentified as beta decay electron.



The difference of A and C z position (mm) The difference of A and C z position (mm)

Figure 3.10: Difference of the z positions between the points A and C for the beta decay electron and  $\pi^0$  in the simulation. In the case of the beta decay electron, the z difference distributes around 0 due to a straight track. In the case of the  $\pi^0$ , the z difference widely distributes because charged particles from the electromagnetic shower in the BGO hit the plastic counters.

### 3.2.5 Photon detector around the SKS spectrometer

By the analysis described above, the remaining backgrounds of  $\pi^0$  and  $\pi^-$  are 12.6 % and 0.16 % of the beta decay electron signal, respectively. The  $\pi^-$  events are rejected well, but the reduction of  $\pi^0$  is not enough. This is because when one photon escapes from the BGO holes in upstream or downstream, one cluster is produced in BGO by the other photon. To reduce such photon leak events, we plan to install photon veto counters around the SKS magnet. In this simulation, photon veto counters are installed at the end of the downstream BGO hole. By the simulation, 70% of remaining  $\pi^0$  events are rejected by vetoing leak photon detection events. Figure 3.11 shows the expected photon veto counter. The materials are lead and plastic scintillator. The photon converts to  $e^-e^+$  in the lead, and they are detected by the plastic counter. We consider the structure of the veto counter made of one layer or two layers. Detailed information and the simulation study for the photon veto counters are shown later.

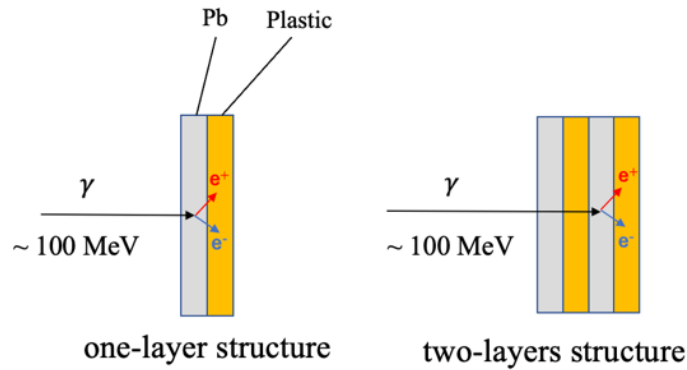


Figure 3.11: The expected photon veto counters to be installed around the SKS magnet. Left shows the detector of one-layer structure (Pb + Plastic), and right shows the detector of two-layers structure.

### 3.2.6 Spectrum of beta decay electron

Table 3.2 shows the reduction rates of detectors and correlation method ( $\Delta z$ ) for the  $\pi^0$  and  $\pi^-$  background events through the analyses with each detector and the correlation method ( $\Delta z$ ). By all the analysis described above, the remaining background is 0.16% ( $\pi^-$ ) + 3.6% ( $\pi^0$ )  $\approx$  4% of the beta decay electrons. This value is almost the same as the required statistical error of the beta decay measurement.

Figure 3.12 shows a simulated energy spectrum of beta decay electron (blue) and the remaining background (red).

Table 3.2: The reduction rates of detectors and correlation method ( $\Delta z$ ) for the  $\pi^0$  and  $\pi^-$  background events through the analyses with each detector and the correlation method ( $\Delta z$ ).

	BR	BGO	Lucite	Plastic	$\Delta z$	Photon counter	(BG)/BR(SIG)
$\pi^0$	0.2	0.03	0.1	0.1	0.8	0.3	0.036 (3.6%)
$\pi^-$	0.4	0.07	0.045	0.001	1	1	0.0026(0.26%)

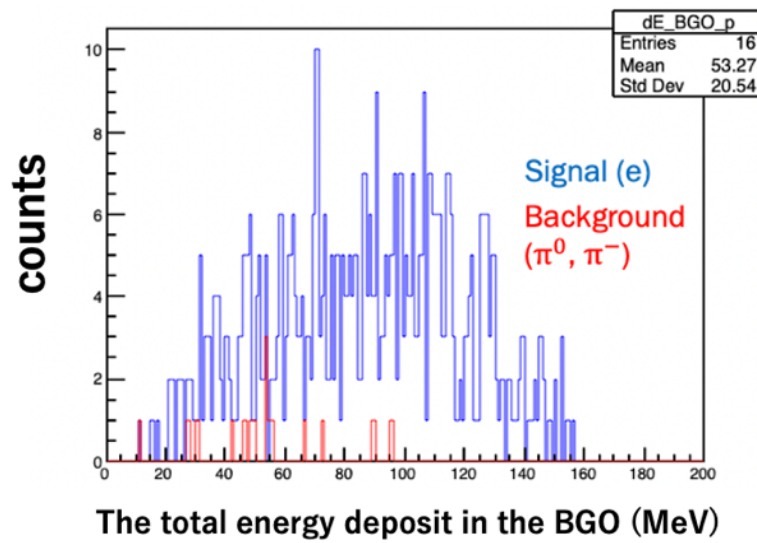


Figure 3.12: Simulated spectrum of the beta decay electron energy (blue) and the remaining background events (red) after all the background reduction analysis (see text).

In our simulation, the background is estimated by the ideal conditions such as fine BGO segments and a large BGO thickness. To show the feasibility of the experiment, the number of segments and the thickness of BGO should be optimized in order to reduce preparation time and cost.

### 3.3 Optimization of BGO counter

The BGO detectors should be optimized considering the preparation time and the cost. Since BGO crystal is expensive, we studied effects of the background rates by changing the number of BGO segments and the thickness of each BGO crystal.

#### 3.3.1 Optimization of the number of segments of BGO

Figure 3.13 shows the relation between the background rate and the number of BGO segments. Here, the background rate was estimated from the number of events which remained after all the background suppression analysis described before. As shown in Figure 3.13, the background rate increases when the number of BGO segments is less than 100. This is because the cluster analysis does not work well for the less segments. Figure 3.14 shows an example of the hit pattern in BGO in the case of 225 segments, and Figure 3.15 shows the case of 49 segments. With respect to the beta decay electron and  $\pi^0$ , the number of clusters does not change by changing the number of segments. However, the number of clusters for  $\pi^-$  changed. In the case of 225 segments,  $\pi^-$  mostly produces two or more clusters. In the case of 49 segments,  $\pi^-$  produces one-cluster. Figure 3.16 shows the number of clusters in the case of 49 segments. As shown in Figure 3.16, the events of the beta decay electron and  $\pi^0$  producing one-cluster events do not increase. However, in the case of  $\pi^-$ , one-cluster events greatly increase as 7.8 % (225 segments)  $\rightarrow$  31 % (49 segments). Therefore, more  $\pi^-$ 's cannot be distinguished from the beta decay electron, and the background from  $\pi^-$  increases under less BGO segments. Finally, we found that the number of BGO segments should be larger than 100.

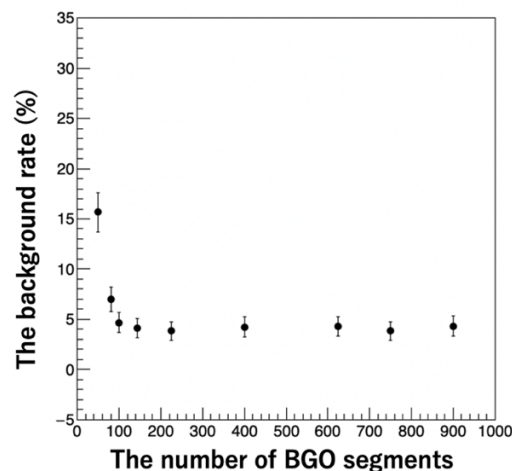


Figure 3.13: Simulated background rate for the beta decay electron as a function of the number of BGO segments. The background rate increases when the number of BGO segments is less than 100 due to worse performance of the cluster analysis.

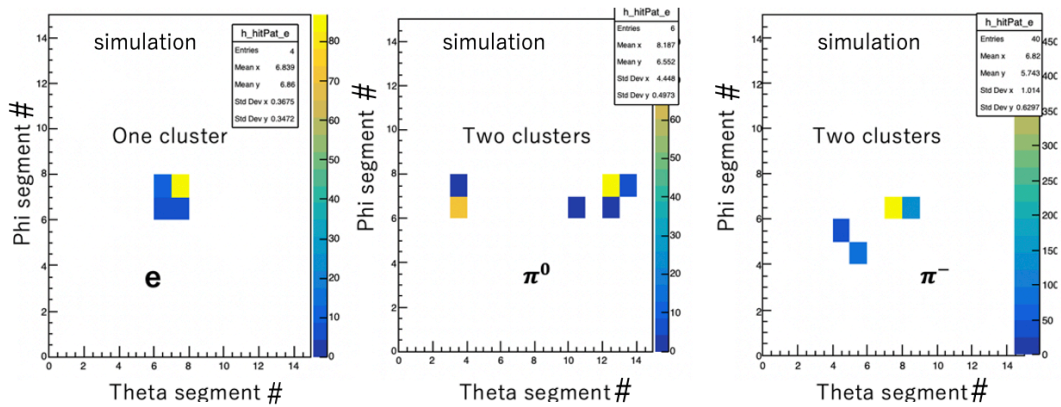


Figure 3.14: An example of the hit pattern of beta decay electron,  $\pi^0$  and  $\pi^-$  in the case of 225 BGO segments in the simulation.

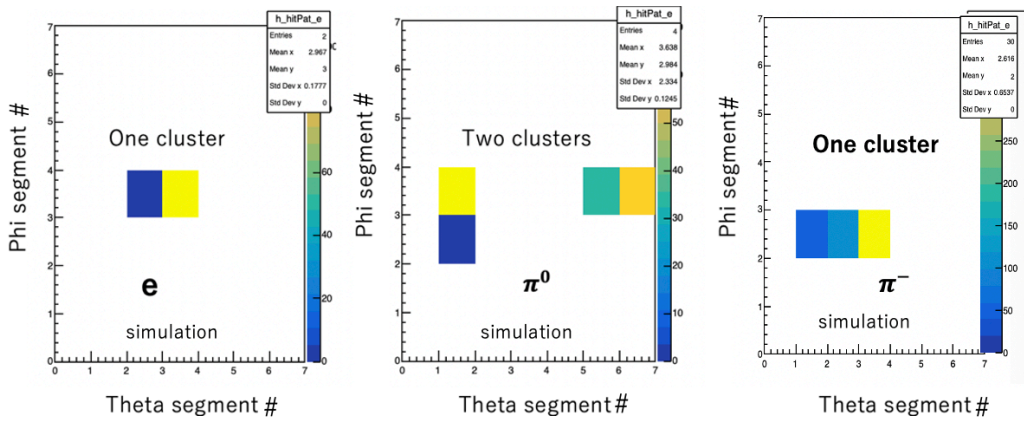


Figure 3.15: An example of the hit pattern of beta decay electron,  $\pi^0$  and  $\pi^-$  in the case of 49 BGO segments in the simulation.

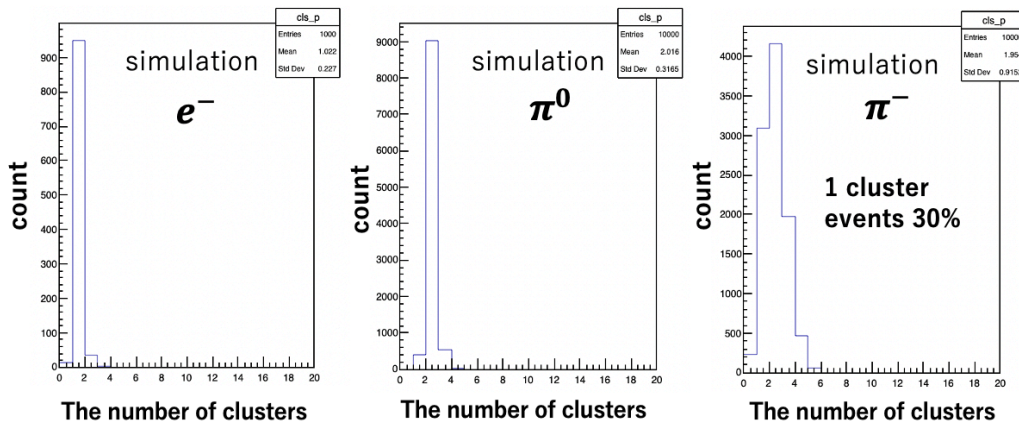


Figure 3.16: The number of clusters in the BGO for the beta decay electron,  $\pi^0$  and  $\pi^-$  in the case of 49 segments (simulation). In the case of the beta decay electron and  $\pi^0$ , one-cluster events do not increase. In the case of  $\pi^-$ , one-cluster events greatly increase as 7.8 % (225 segments)  $\rightarrow$  31 % (49 segments).

### 3.3.2 Optimization of the thickness of BGO

Figure 3.17 shows the relation between the background rate and the thickness of BGO. Here, the background rate was estimated from the number of events which remained after all the background suppression analysis described before. As shown in Figure 3.17, the background rate increases for the thickness less than 20 cm. Figure 3.18 shows an example of the hit pattern in BGO of  $\pi^-$  with a 10 cm thickness and a 30 cm thickness. As shown in Figure 3.18, the number of clusters decreases by reducing the BGO thickness (30 cm  $\rightarrow$  10 cm). Since the reaction rate of neutron is proportional to the BGO thickness, neutrons from  $\pi^-$  produce fewer clusters in the case of 10 cm BGO thickness than 30 cm thickness. Finally, we found that the BGO thickness should be more than 20 cm.

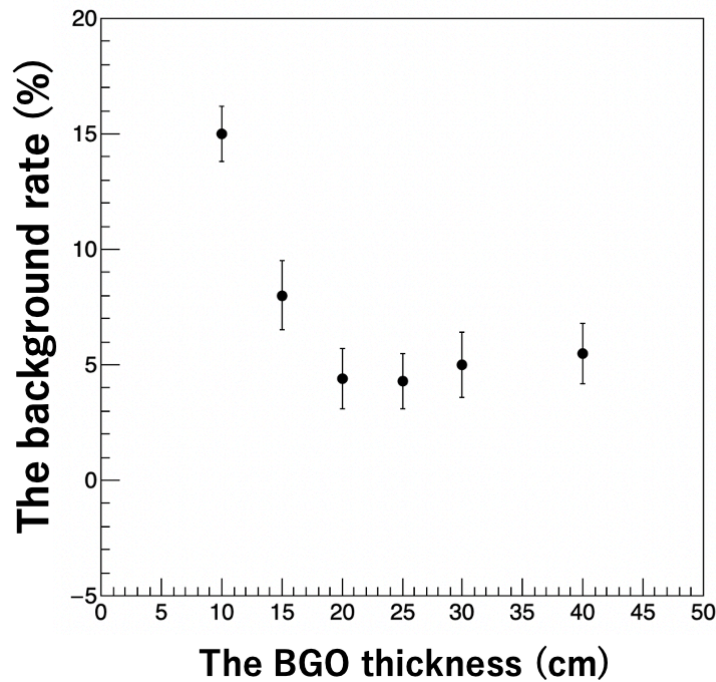


Figure 3.17: Simulated background rate of the beta decay electron as a function of the BGO thickness. The background rate increases for the BGO thickness less than 10 cm due to reduction of the neutron reaction rate.

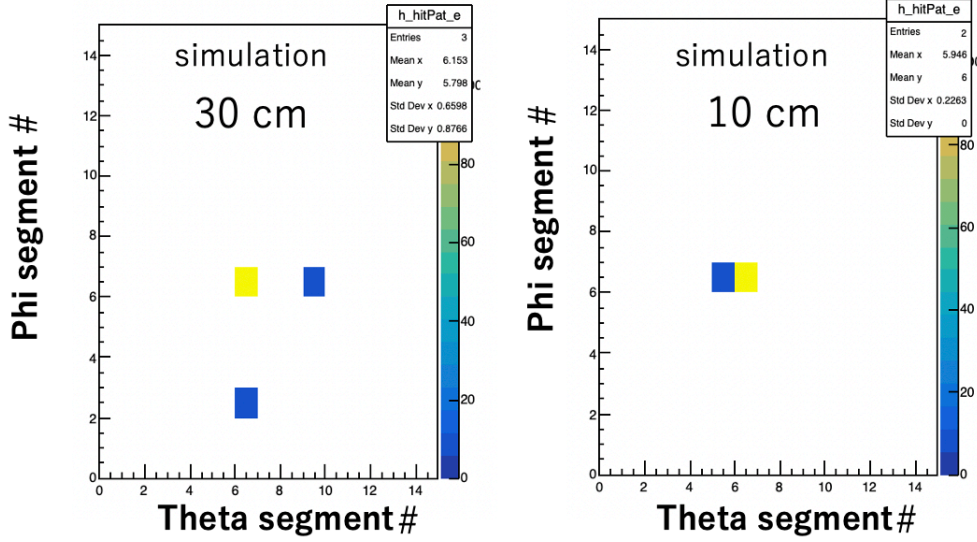


Figure 3.18: An example of the simulated hit pattern in the BGO calorimeter for  $\pi^-$  in the case of 10 cm and 30 cm BGO thickness. Due to reduction of the neutron reaction rate, the number of clusters decrease as 3 clusters  $\rightarrow$  1 cluster.

### 3.4 Optimization of the photon veto counter in SKS

In the previous  $\pi^0$ ,  $\pi^-$  simulation, we installed photon veto counters which cover all the solid angle of the BGO downstream hole. However, in reality, the photon veto counters made of plastic and lead sheets as shown in Figure 3.11 are installed on the wall of the entrance of SKS magnet and on the pole face of the SKS magnet. In addition, the real detection rate of photon is not 100%. Since the shape and the size of the counters depend on the installed position, we optimized only the thickness of the photon veto counter. In the simulation, we assumed that the maximum thickness is 20 mm because the acceptance of the SKS magnet for the scattered kaons decreases by the photon veto counter. The thickness of the plastic counter is assumed to be 5 mm, and MPPCs to read a signal are attached at both ends of the plastic. We studied the detection rate of photon by changing the thickness of lead. Figure 3.19 shows the relation between the detection rate of 100 MeV photon and the thickness of lead (5mm ~ 15mm) in the case of one-layer structure. As shown in Figure 3.19, the detection rate saturates at about 60% over 10 mm. Therefore, the thickness should be more than 5 mm (plastic) + 10 mm (lead) = 15 mm if photon detector has one- layer. In the case of two-layers structure, we studied 3, 4, 5 mm-thick lead (16 mm, 18 mm, 20 mm thick in total). The detection rates are found to be 64 %, 56% and 47%, respectively. In conclusion, detection rate of photon detector is 64 % at maximum with the photon veto counters of two-layers structure. In near future, we will

study 3, 4-layers structure, and more realistic design will be made depending on the installed position.

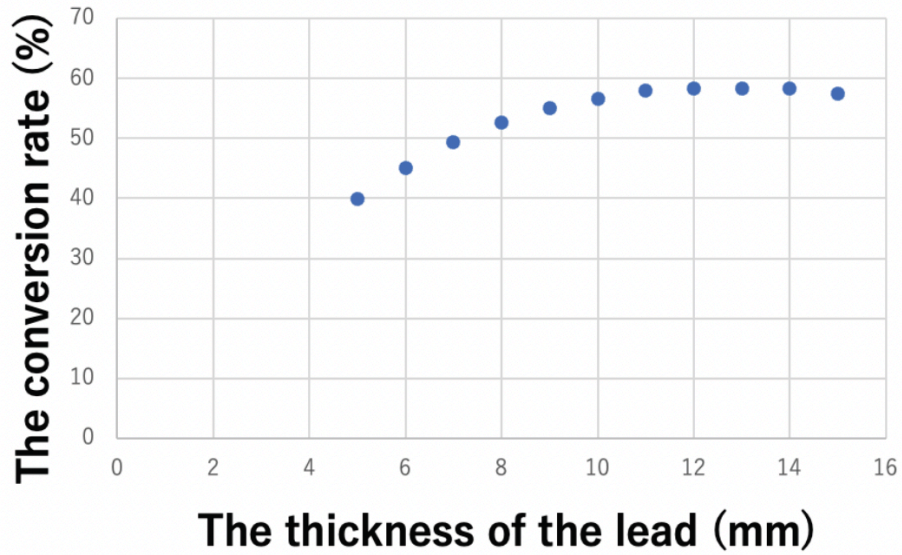


Figure 3.19: The relation between the detection rate of 100 MeV photon and the thickness of the lead (5mm ~ 15mm) in the case of one-layer structure (simulation).

## 3.5 Study of other background

### 3.5.1 Nonmesonic weak decay of $\Lambda$

Since a  $\Lambda$  is in a nucleus, non-mesonic weak decay (NMWD) may become background. NMWD in  ${}^5\Lambda\text{He}$  was measured in the KEK E462 experiment, and the total kinetic energy of np and nn pair are shown in Figure 1.5. Figure 3.20 (a) and (b) show the angle between the nucleon pair. The angle between neutron and proton distributes around  $\pi$  (rad). In the present GEANT4 simulation, the total kinetic energy of np pair is randomly selected in the range of 100 – 160 MeV (see Section 1.3), and the pair particles are produced back to back from the target. The number of nn and np pairs is determined according to the measured branching ratio shown in Table 1.1.

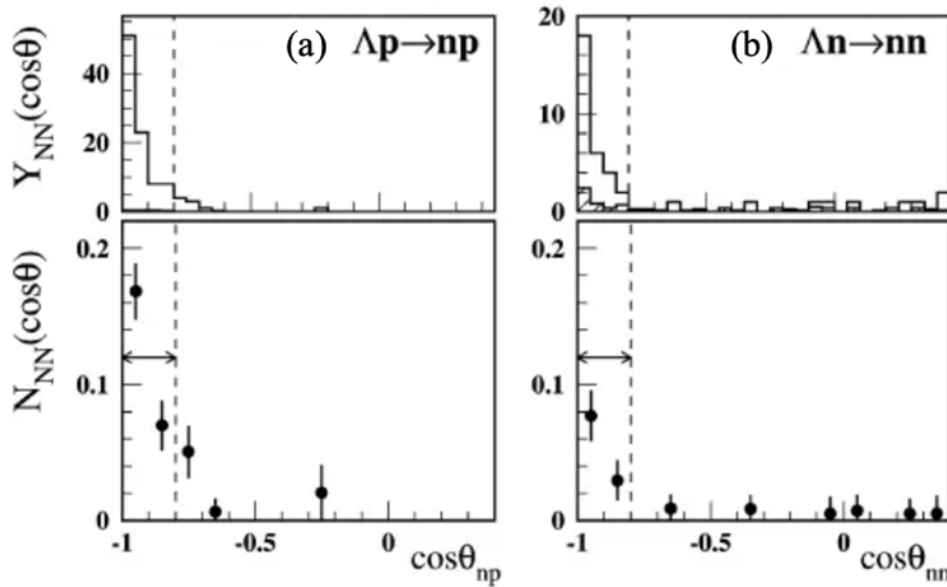
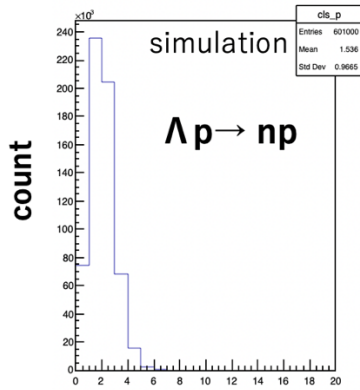


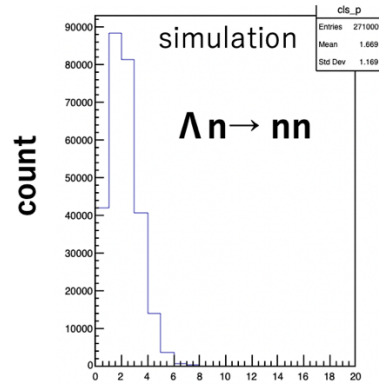
Figure 3.20 (a), (b): Measured angle between neutron-proton pair and neutron-neutron pair in the KEK E462 experiment. The angle distribute at almost  $\pi$  (rad). Thus, we regard the angle between two nucleons as  $180^\circ$  (back to back in the simulation) [13].

### 3.5.2 Reduction of nonmesonic weak decay of $\Lambda$

At first, the background of NMWD is reduced via the cluster analysis in BGO. Figure 3.21 shows the number of clusters in BGO for  $\Lambda p \rightarrow np$  and  $\Lambda n \rightarrow nn$  events. As shown in Figure 3.21, both  $\Lambda p \rightarrow np$  and  $\Lambda n \rightarrow nn$  produce several clusters. By selecting one-cluster events, 61% of  $\Lambda p \rightarrow np$  and 67% of  $\Lambda n \rightarrow nn$  events are rejected.



The number of clusters in the BGO

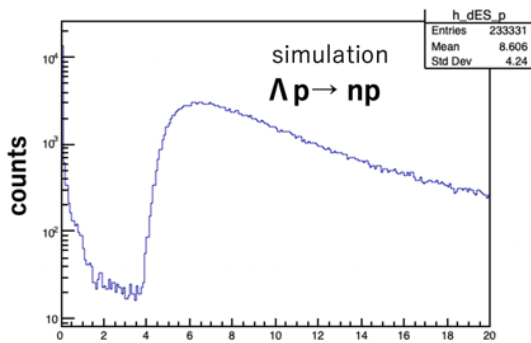


The number of clusters in the BGO

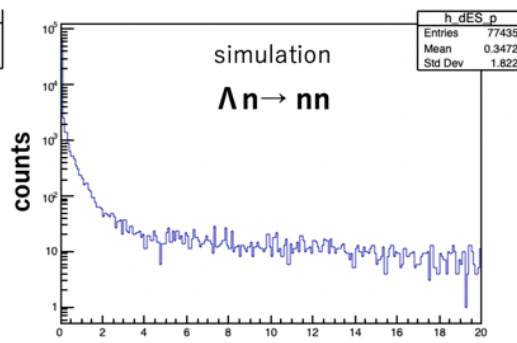
Figure 3.21: The number of clusters in BGO for  $\Lambda p \rightarrow np$  and  $\Lambda n \rightarrow nn$  in the simulation. Both  $\Lambda p \rightarrow np$  and  $\Lambda n \rightarrow nn$  produce several clusters.

Further reduction of background can be made by the analysis with the plastic counters. Figure 3.22 shows the energy deposit in the plastic counters for  $\Lambda p \rightarrow np$  and  $\Lambda n \rightarrow nn$ . Both energy loss spectra widely distribute. In addition, Figure 3.23 shows the energy deposit per path length in the plastic counters. After selecting 0.7 – 3.0 MeV as the beta decay electron in the total energy loss spectrum in the plastic counter, 99.8% of  $\Lambda p \rightarrow np$  and 98% of  $\Lambda n \rightarrow nn$  events are rejected by selecting 0.12 – 0.27 MeV/mm as the beta decay electron.

In addition, 99.5% of  $\Lambda p \rightarrow np$  and 95.4 % of  $\Lambda n \rightarrow nn$  events are rejected by the analysis in the lucite Cerenkov counters since the velocities of most of the nucleons from NMWD are small ( $\beta < 0.4$ ).



The total energy deposit in plastic  $\Delta E$  (MeV)



The total energy deposit in plastic  $\Delta E$  (MeV)

Figure 3.22: The total energy deposit in the plastic counter for  $\Lambda p \rightarrow np$  and  $\Lambda n \rightarrow nn$  in the simulation. In both cases, the energy distributes widely, and they can be rejected well by selecting the MIP region for the beta decay electron.

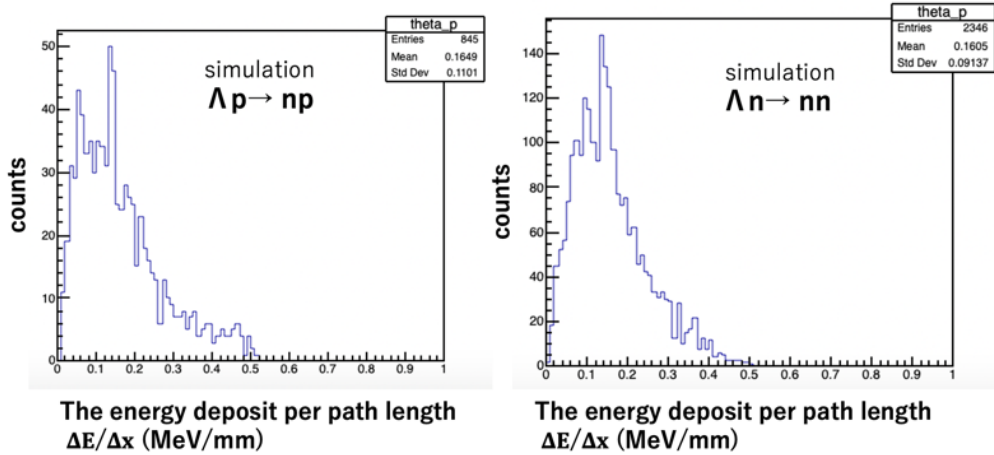


Figure 3.23: The energy deposit per path length in the plastic counter for  $\Lambda p \rightarrow np$  and  $\Lambda n \rightarrow nn$  after selecting 0.7 – 3 MeV as the beta decay electron in the total energy deposit (simulation).

More analyses are carried out, and then Figure 3.24 shows the total energy spectrum of the remaining np and nn events, respectively. The rate of nn and np events to the beta decay electron are 4 % and 2%, respectively. The energy distributes in the region less than 40 MeV in both  $\Lambda p \rightarrow np$  and  $\Lambda n \rightarrow nn$ , as shown in Figure 3.24. Remaining events can be rejected further by cutting events under 40 MeV, but beta decay electron events are also cut. We plan to determine the energy threshold by considering beta decay electron and other backgrounds.

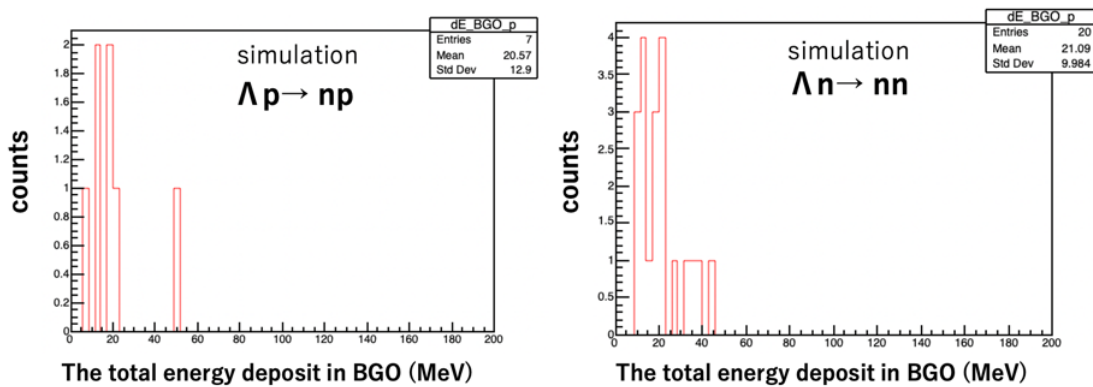


Figure 3.24: Simulated energy spectra in BGO of remaining  $\Lambda p \rightarrow np$  and  $\Lambda n \rightarrow nn$  events. The rate of background ( $\Lambda p \rightarrow np + \Lambda n \rightarrow nn$ ) to the beta decay electron signal is  $4\% + 2\% = 6\%$ .

### 3.5.3 $\mu^-$ from three body decay of $\Lambda$

Since the branching ratio of  $\Lambda \rightarrow p\mu^- \bar{\nu}_\mu$  is 20% of that of the beta decay, muons may become background. Figure 3.25 shows calculated kinetic energy and velocity distribution of muons in the  $\Lambda \rightarrow p\mu^- \bar{\nu}_\mu$  decay. As shown in Figure 3.25, the kinetic energy distributes in 0 – 75 MeV, and the velocity distributes in 0 – 0.8. 74% of muons are rejected by the lucite Cerenkov counter. We studied the muon background in the GEANT4 simulation as well as other background and found that 99.4 % of muon events are rejected. The rate of muon to the beta decay electron signal becomes  $20\% \times 0.006 = 0.12\%$ . In conclusion, muon does not become a problem for the beta decay experiment.

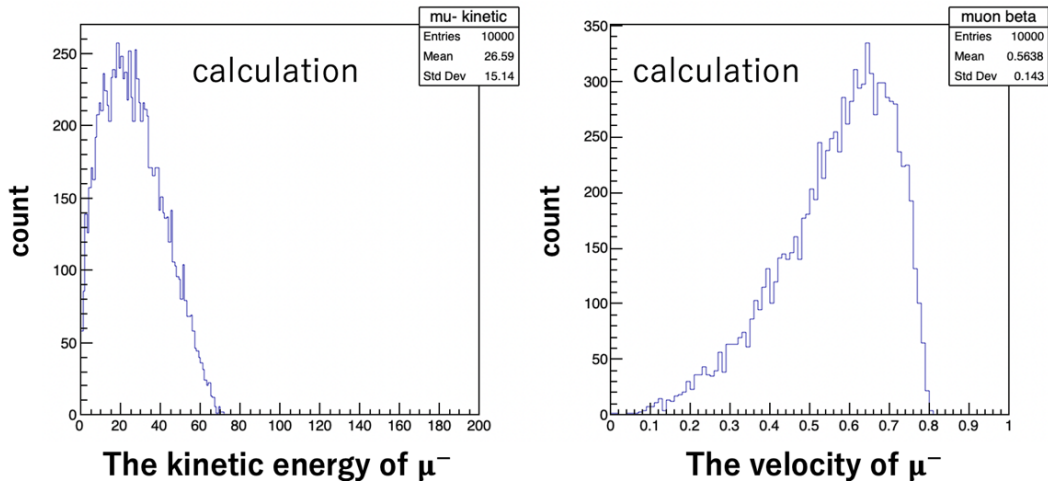


Figure 3.25: Calculated spectra of the kinetic energy and the velocity of muons in the  $\Lambda \rightarrow p\mu^- \bar{\nu}_\mu$  decay. The kinetic energy distributes in 0 – 75 MeV, and the velocity distributes in 0 – 0.8.

### 3.5.4 Quasi-free $\Lambda$

As shown in Figure 3.26 quasi-free  $\Lambda$  (Q-F  $\Lambda$ ) production events contaminate the ground state of  ${}^6_\Lambda\text{Li}$  in the missing mass spectrum, and they may produce background for the  $\Lambda$  in  ${}^5_\Lambda\text{He}$ . In the KEK E462 experiment, events with excitation energy  $-5 \text{ MeV} \leq E_{\text{ex}} \leq 5 \text{ MeV}$  are identified as the production of  ${}^6_\Lambda\text{Li}$  ground state. Therefore, we simulated events momentum of Q-F  $\Lambda$  whose  $E_{\text{ex}}$  meets  $-5 \text{ MeV} \leq E_{\text{ex}} \leq 5 \text{ MeV}$  in GEANT4.

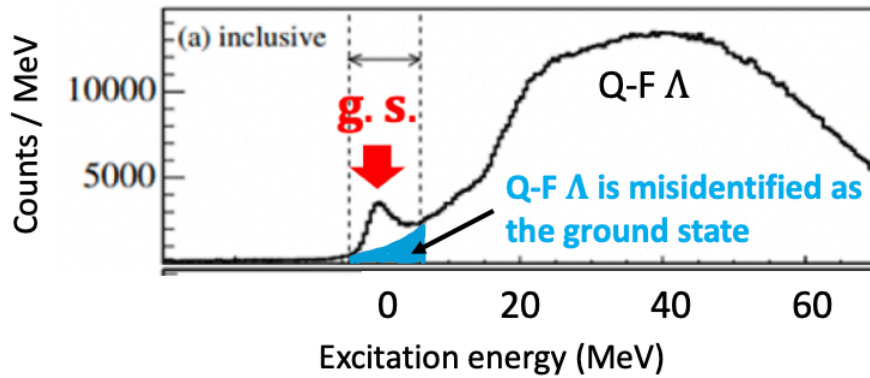
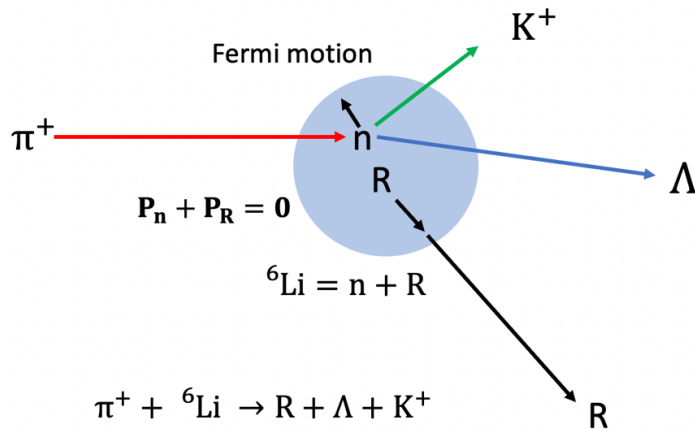


Figure 3.26: Missing mass spectra of production of  ${}^6_\Lambda\text{Li}$  and quasi-free  $\Lambda$  (Q-F  $\Lambda$ ). Q-F  $\Lambda$  events contaminate the ground state of  ${}^6_\Lambda\text{Li}$ .

Figure 3.27 shows the schematic view of Q-F  $\Lambda$  production. Beam  $\pi^+$  hits a neutron in  ${}^6\text{Li}$ , and then  $K^+$  and Q-F  $\Lambda$  are produced. In this reaction, we expect that  ${}^6\text{Li}$  is composed of neutron and the residual core R ( ${}^5\text{Li}$ ), and they have fermi momenta  $\mathbf{P}_n$  and  $\mathbf{P}_R$ , respectively. We used the momentum distribution of the neutron in  ${}^{12}\text{C}$  measured by  ${}^{12}\text{C}(e, e'p)$  reaction as shown in Figure 3.28 [22].



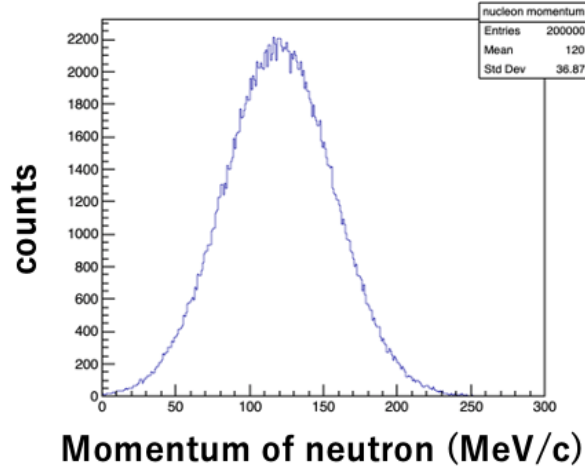


Figure 3.28: The momentum distribution of the neutron in  $^{12}\text{C}$  measured by  $^{12}\text{C}(e, e'p)$  reaction [22]. The residual core has the same momentum as the neutron.

Conservations of energies and momenta are written as follows.

$$\mathbf{P}_\pi + \mathbf{P}_n + \mathbf{P}_R = \mathbf{P}_R + \mathbf{P}_\Lambda + \mathbf{P}_K \quad (\text{i})$$

$$E_\pi + E_n + E_R = E_R + E_\Lambda + E_K \quad (\text{ii})$$

By subtracting  $\mathbf{P}_R$ ,  $E_R$  (we expect that R is not affected in this reaction), the equations (i), (ii) are given as

$$\mathbf{P}_\pi + \mathbf{P}_n = \mathbf{P}_\Lambda + \mathbf{P}_K \quad (\text{i})$$

$$E_\pi + E_n = E_\Lambda + E_K \quad (\text{ii}).$$

In this calculation, we adjusted the mass of the neutron to satisfy  $E_n + E_R = M_C$ , where  $M_C$  is the mass of  $^6\text{Li}$ . The effective mass of neutron  $M_n^*$  is given as

$$M_n^* = \sqrt{M_C^2 + M_R^2 - 2M_C \sqrt{M_R^2 + \mathbf{p}_R^2}} \quad .$$

To calculate the momentum of  $\Lambda$  in  $\pi^+n \rightarrow K^+\Lambda$ , we consider the CM system first. Here, Figure 3.29 shows  $\pi^+n \rightarrow K^+\Lambda$  reaction in Lab and CM systems, respectively.

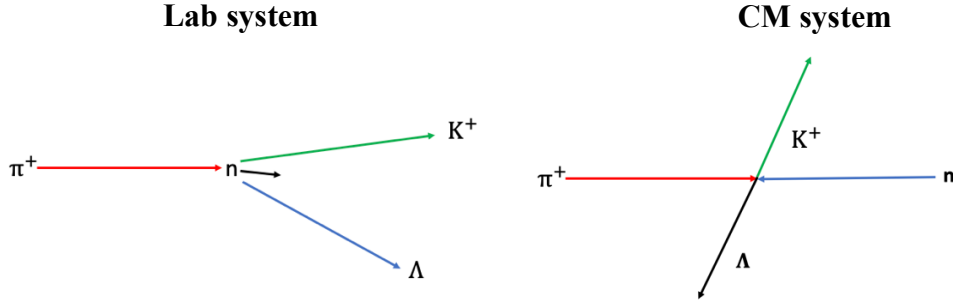


Figure 3.29:  $\pi^+n \rightarrow K^+\Lambda$  reaction in the Lab and the CM systems. Considering the CM system, the momentum of the beam  $\pi^+$  and the neutron are the same, and the scattered  $K^+$  and the Q-F  $\Lambda$  also have the same momentum.

Considering the CM system, the momenta of the beam  $\pi^+$  and the neutron are the same.  $K^+$  and Q-F  $\Lambda$  also have the same momentum, and their momenta are calculated to be

$$|P_\Lambda| = |P_K| = \sqrt{\left(\frac{M^2 + M_K^2 - M_\Lambda^2}{2M}\right)^2 - M_K^2}.$$

$M_K$  and  $M_\Lambda$  are the mass of  $K^+$  and  $\Lambda$ .  $M$  is the total energy of the beam  $\pi^+$  and the neutron in the CM system.  $M$  is the invariant mass under the Lorentz transformation. It is given as

$$M^2 = (E_\pi + E_n)^2 - (\mathbf{P}_\pi + \mathbf{P}_n)^2 = M_\pi^2 + M_n^2 + 2(E_\pi E_n - \mathbf{P}_\pi \cdot \mathbf{P}_n).$$

$M_\pi$  and  $M_n$  are the mass of  $\pi^+$  and the neutron. We expect that  $|\mathbf{P}_\pi|$  is 1.1 GeV/c (K1.1 beamline), and  $\mathbf{P}_n$  has a random direction with fermi momentum of  $|\mathbf{P}_n|$ . Converting the CM system to the Lab system by using beta of CM system  $\beta_{CM}$ ,

$$\beta_{CM} = \frac{\mathbf{P}_\pi + \mathbf{P}_n}{E_n + E_\pi}$$

the momentum of  $K^+$  and  $\Lambda$  are calculated. The reaction points of  $\pi^+n \rightarrow K^+\Lambda$  are uniformly generated in the Li target, and the direction of  $\mathbf{P}_n$  are also uniformly generated. After calculating, we selected the events of  $K^+$  which escaped from the BGO downstream hole to reproduce  $(\pi^+, K^+)$  reaction in our calculation.

Figure 3.30, 3.31 shows the calculated momentum of Q-F  $\Lambda$  and the reaction point for x, y, z directions. As shown in Figure 3.30, momenta of x,y direction widely distributes, and that of z distributes over 400 MeV/c. As shown in Figure 3.31, x, y position distributes

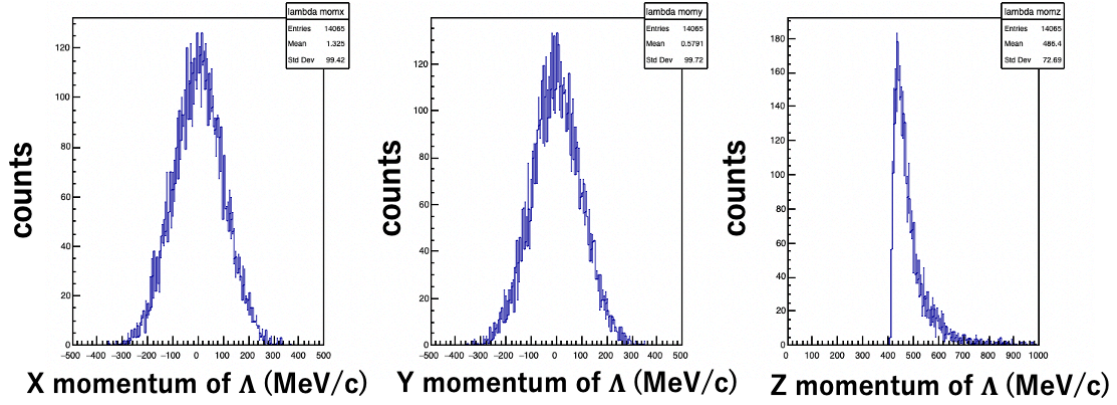


Figure 3.30: Calculated momentum distributions of Q-F  $\Lambda$  for x, y, z directions. Momentum of x and y direction distributes around 0 MeV/c, and momentum of z distributes more than 400 MeV/c.

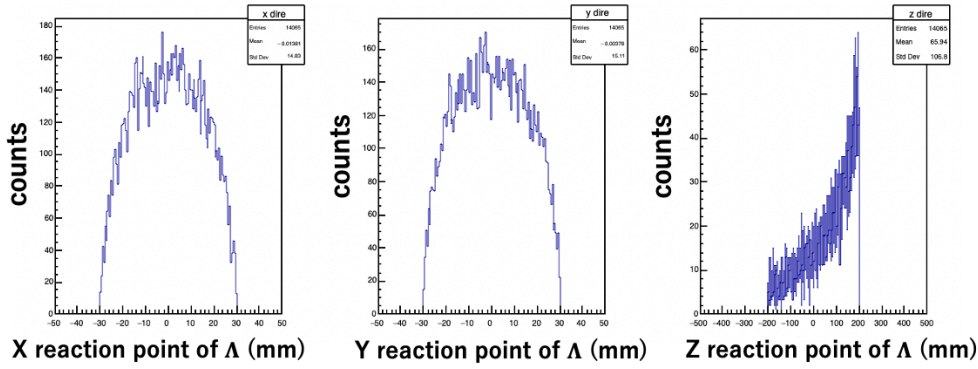


Figure 3.31: Calculated distributions of  $\Lambda$ 's generation points for x, y, z directions. z position concentrates at 200 mm.

around 0 mm, and z position concentrates at 200 mm (near BGO downstream hole). However, we have to consider the Q-F  $\Lambda$  whose excitation energy  $-5 \text{ MeV} \leq E_{\text{ex}} \leq 5 \text{ MeV}$ , we calculate  $E_{\text{ex}}$  via

$$E_{\text{ex}} = \sqrt{M_{\Lambda}^2 + M_R^2 + 2E_{\Lambda}E_R - 2\mathbf{P}_{\Lambda} \cdot \mathbf{P}_R} - (M_{\Lambda} + M_R - B_{\Lambda}).$$

Figure 3.32 shows the excitation energy  $E_{\text{ex}}$  of calculated Q-F  $\Lambda$ . We can see that  $E_{\text{ex}}$  distributes widely, and it has peak at 0 MeV. We selected  $-5 \text{ MeV} \leq E_{\text{ex}} \leq 5 \text{ MeV}$ , and obtained momenta and reaction points of Q-F  $\Lambda$  which are misidentified as the bound state  $\Lambda$ . Then, we generated these eventd in GEANT4 and simulated effects from Q-F  $\Lambda$  on

measuring the beta decay electron. Figure 3.33, 3.34 shows calculated momentum of Q-F  $\Lambda$  and reaction point for x, y, z directions after selecting  $-5 \text{ MeV} \leq E_{\text{ex}} \leq 5 \text{ MeV}$ .

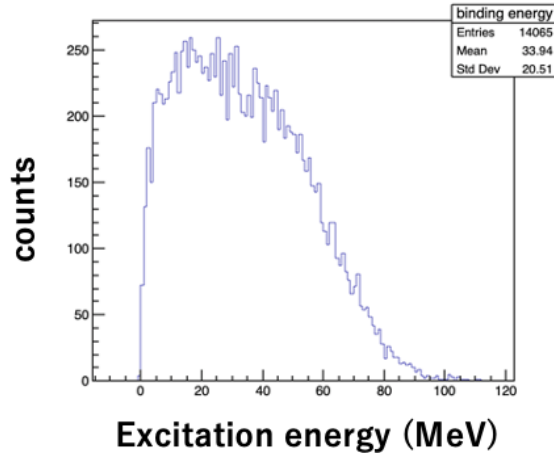


Figure 3.32: The excitation energy of calculated Q-F  $\Lambda$ . The energy distributes widely and concentrates at 0 MeV.

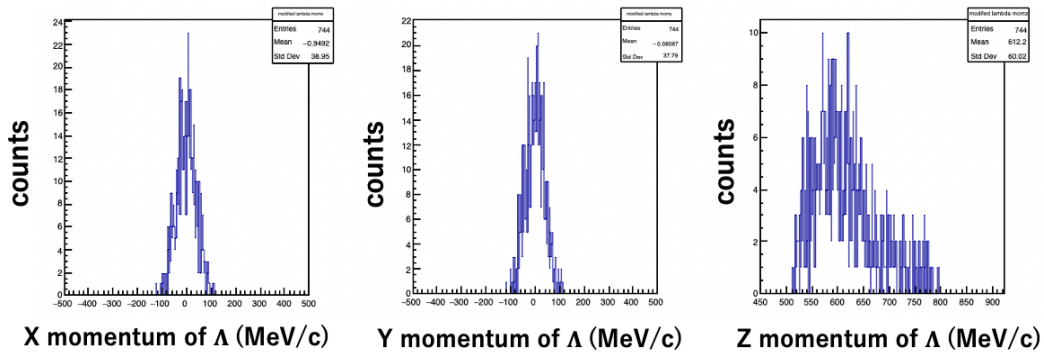


Figure 3.33: Calculated momentum distributions of Q-F  $\Lambda$  for x, y, z directions after selecting  $-5 \text{ MeV} \leq E_{\text{ex}} \leq 5 \text{ MeV}$ .

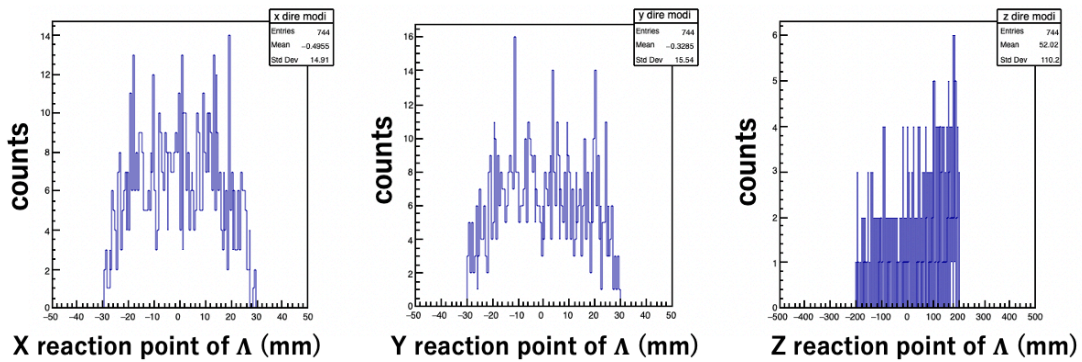


Figure 3.34: Calculated distributions of  $\Lambda$ 's generation points for x, y, z directions after selecting  $-5 \text{ MeV} \leq E_{\text{ex}} \leq 5 \text{ MeV}$ .

### 3.5.5 Reduction of quasi-free $\Lambda$

At first, the background of Q-F  $\Lambda$  is reduced via the cluster analysis in BGO. Figure 3.35 shows the hit pattern and the number of clusters in BGO. By selecting one-cluster events, 82% of Q-F  $\Lambda$  events are rejected.

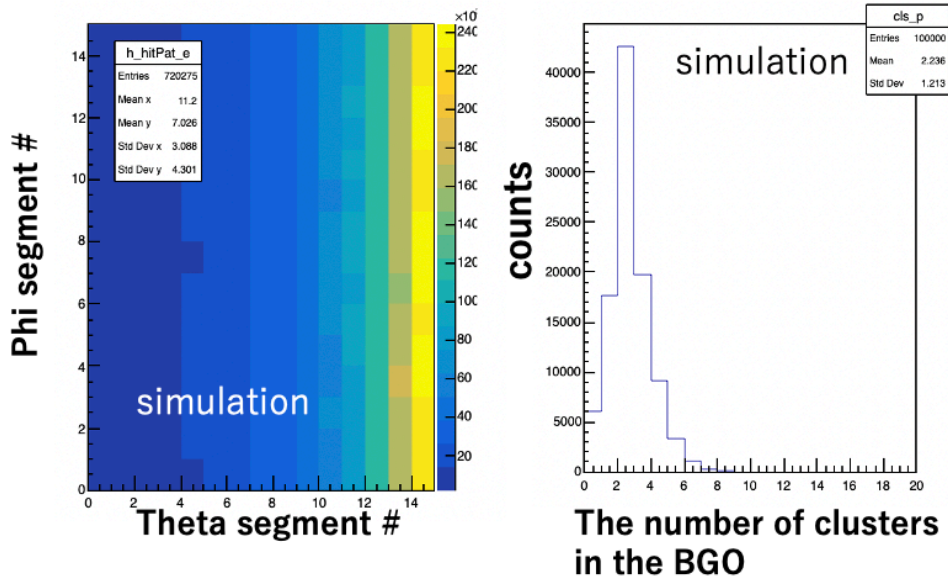


Figure 3.35: The hit pattern and the number of clusters in BGO for Q-F  $\Lambda$  in the simulation. Q-F  $\Lambda$  produces several clusters.

In addition, 57% of Q-F  $\Lambda$  events are rejected by the analysis in the lucite Cerenkov counters. This reduction rate is worse in comparison with that of  $\Lambda$  in  ${}^5\text{He}$ . This is because  $\pi^-$  from mesonic weak of Q-F  $\Lambda$  decay has a faster velocity than that of  $\Lambda$  in  ${}^5\text{He}$ .

Further reduction of background can be made by the analysis with the plastic counters. Figure 3.36 shows the energy deposit in the plastic counters. The energy loss spectrum widely distributes. In addition, Figure 3.37 shows the energy deposit per path length in the plastic counters. After selecting 0.7 – 3.0 MeV as the beta decay electron in the total energy loss spectrum in the plastic counter, 98.1% of Q-F  $\Lambda$  events are rejected by selecting 0.12 – 0.27 MeV/mm as the beta decay electron.

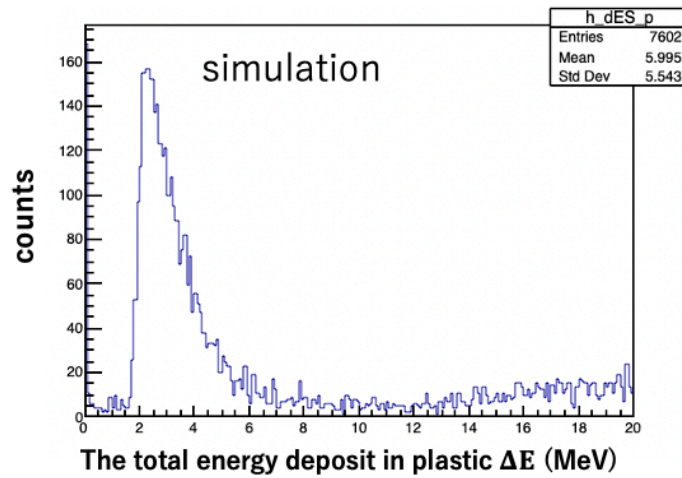


Figure 3.36: The total energy deposit in the plastic counter for Q-F  $\Lambda$  in the simulation. The energy distributes widely.

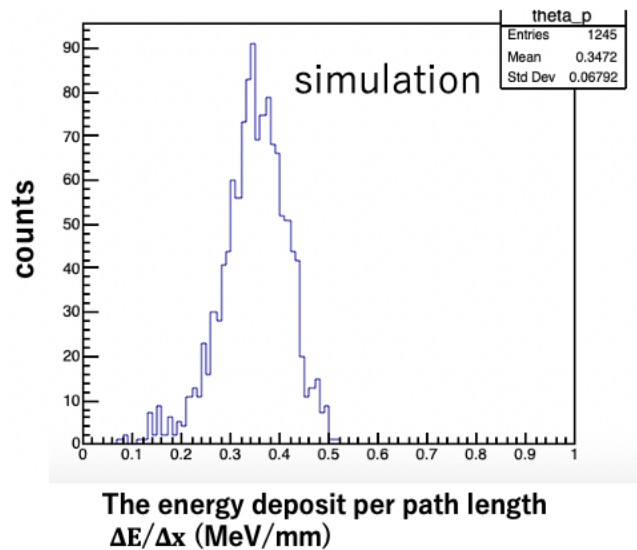


Figure 3.37: The energy deposit per path length in the plastic counter for Q-F  $\Lambda$  after selecting 0.7 – 3 MeV as the beta decay electron in the total energy deposit (simulation).

More analyses are carried out, and then Figure 3.38 shows the total energy spectrum of the remaining Q-F  $\Lambda$  events. The rate of Q-F  $\Lambda$  events to the beta decay electron is 11.9%. However, as shown in Figure 3.38 the energy distributes in the region more than maximum kinetic energy of beta decay electron (163 MeV), thus remaining events can be rejected further by selecting the energy less than 163 MeV. By this selection, 16% of remaining Q-F  $\Lambda$  events are rejected. This corresponds to 7% background rate for the beta decay electron.

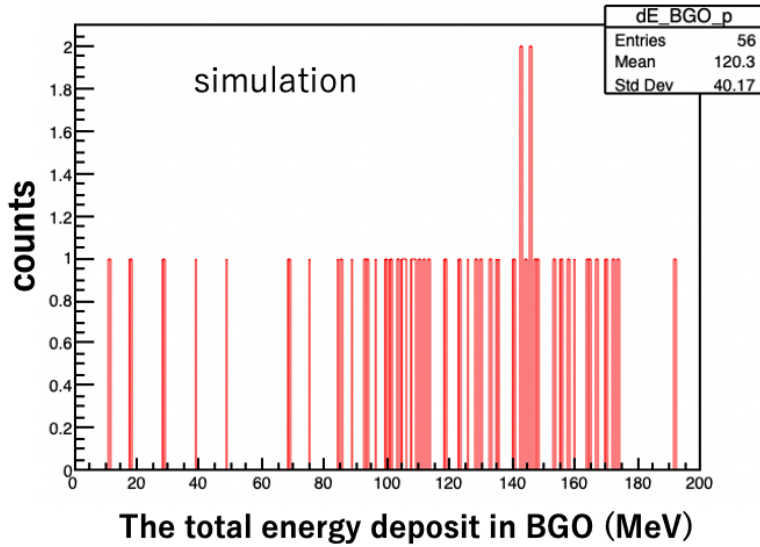


Figure 3.38: Simulated energy spectrum in BGO of remaining Q-F  $\Lambda$  events. The rate of the background to the beta decay electron signal is 14.3%. By selecting the energy less than 163 MeV, the rate is reduced down to 10.5%.

To reduce more remaining events, we used the theta segment number which is the center of one-cluster in the BGO as shown in Figure 3.39. We can see that the center theta segment number distributes around #14 (downstream of BGO) due to the high  $z$  momentum of Q-F  $\Lambda$ . Thus, if events with high theta number hit is rejected, more remaining events can be rejected. However, this selection also cuts the beta decay electron with uniform theta number distribution. When #14 hit events are rejected as the Q-F  $\Lambda$  hit, the background rate is reduced down to 5.9% (6.7% beta decay electron events are rejected, and the statical error become 3.8% (no cut)  $\rightarrow$  3.99%). Furthermore, when #13 and #14 hit events are rejected, the background rate is reduced down to 5.5% (13.4% beta decay electron events are rejected, and the statical error become 3.99%  $\rightarrow$  4.14%). Therefore, #13 and #14 reduction is the limit of Q-F  $\Lambda$  considering the goal of statical error of the beta decay electron (4%). In conclusion, we found that Q-F  $\Lambda$  events do not become a severe problem by rejecting high theta number hit in the BGO. In near future, we will simulate Q-F  $\Lambda$  by considering the mass resolution of hypernucleus.

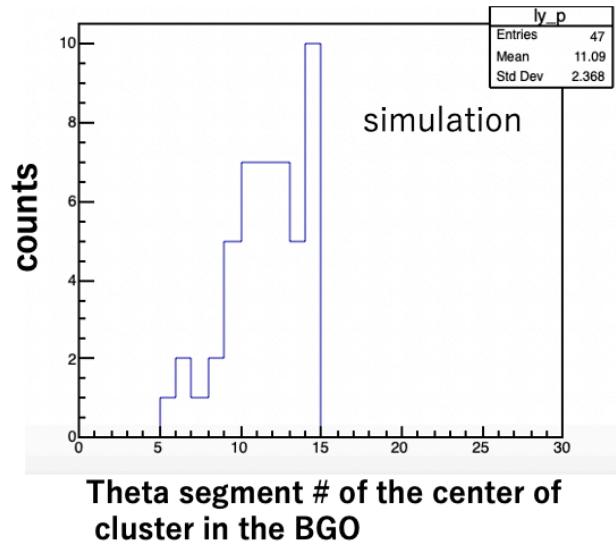


Figure 3.39: The theta segment number of the center of one-cluster in the BGO.

### 3.6 Effects from beam $\pi^+$

Since the intensity of beam  $\pi^+$  is high ( $\sim 10^7/s$ ), a lot of particles from interactions of beam  $\pi^+$  and the Li target are expected to enter the BGO crystal in a high counting rate. BGO is an inorganic scintillator with a large atomic number, and the time response is quite slow (the decay time constant scintillation is  $\sim 1 \mu s$ ). Thus, the BGO detector cannot operate correctly at a rate more than  $10^5$  counts per sec. Therefore, we studied beam  $\pi^+$  effects on the BGO counting rate by a GEANT4 simulation. Figure 3.40 shows the counts of each of the BGO segments with more than 1 MeV energy loss for various theta positions when  $10^5 \pi^+$  beam particles are injected to the target. The number of BGO segments are 225. When  $10^5 \pi^+$ 's are produced in this simulation, more than  $10^3$  counts in a BGO segment correspond to  $10^5$  counts per sec in a real experiment. As shown in Figure 3.40, most of BGO segments have counts over  $10^3$ .

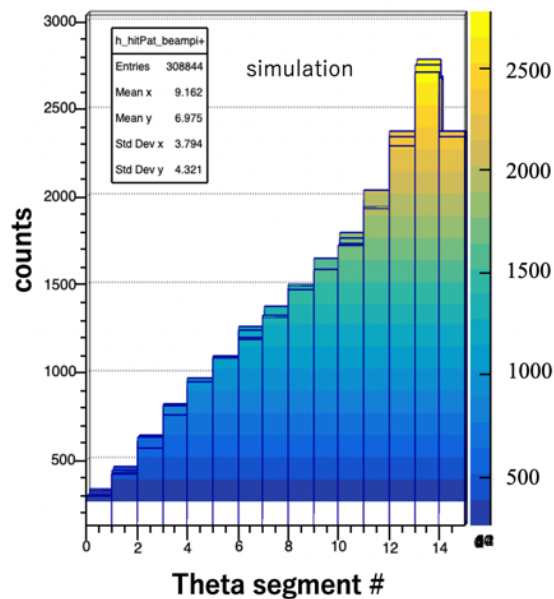


Figure 3.40: BGO counting rate with more than 1 MeV as a function of segment theta number in the simulation.

Figure 3.41 shows the fraction of the number of BGO segments with more than  $10^3$  counts ( $n$ ) out of all the BGO segments of 225 ( $N$ ) as a function of the energy threshold in the simulation. We found that the fraction can be reduced to 24% when the energy threshold is 10 MeV. Figure 3.42 shows fraction of the BGO segments with more than  $10^3$  counts ( $n$ ) out of all the BGO segments of 225 ( $N$ ) as a function of the total number of BGO segments in the simulation. We found that the fraction can be reduced to 15%

when the number of segments is 400. In conclusion, with 10 MeV energy threshold and 400 BGO segments, 15 % BGO segments have more than  $10^3$  counts. These segments should be replaced by fast response scintillator in the real experiment.

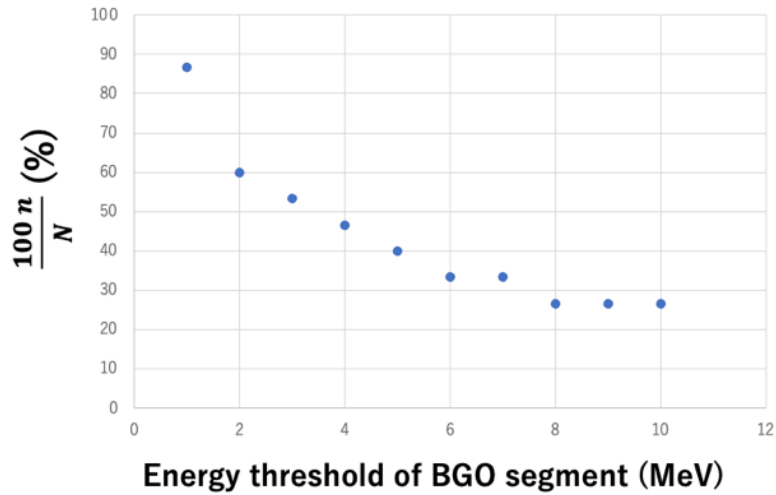


Figure 3.41: Fraction of the number of BGO segments with more than  $10^3$  counts (n) out of all the BGO segments of 225 (N) as a function of the energy threshold in the simulation.

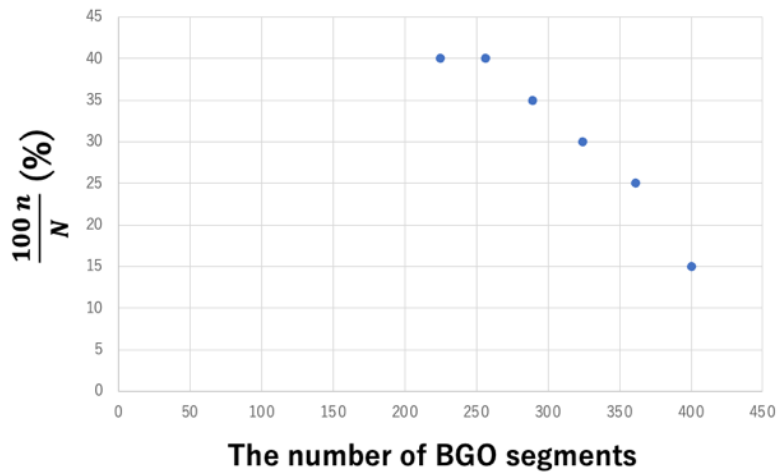


Figure 3.42: Fraction of the number of BGO segments with more than  $10^3$  counts (n) out of all the BGO segments of 225 (N) as a function of the number of BGO segments in the simulation.

## 4 Feasibility of the beta decay experiment

### 4.1 Yield and accuracy of branching ratio of beta decay

Via the background suppression study in Chapter 3, the background rate from the  $\Lambda$ 's main decay mode can be reduced down to 4% (mesonic) + 6% (nonmesonic) + 5.5% (Q-F) = 15.5% of the beta decay signal with the cut of 30 % beta decay electron events. if the remaining background can be subtracted within 30% accuracy, the systematic error of the background for the beta decay electron become  $\sim 5\%$  (30% is roughly estimated). In order to measure the beta-decay branching ratio with a statistical error of 4% (the same as the expected systematic error of  $\sim 4\%$  from the background), more than 625 counts of the beta decay electron events should be measured. Table 4.1 shows the yield of the KEK 462 experiment and the expected yield of the proposed beta decay experiment. The E462 experiment was carried out with  $2.5 \times 10^{12}$   $\pi^+$  on a  $3.7\text{g/cm}^3$   ${}^6\text{Li}$  target, and 45653  ${}^5_{\Lambda}\text{He}$  events were obtained. Since our beta decay experiment will use the same setup for the  $\text{K}^+$  spectrometer as the KEK E462 experiment, we can estimate the number of  ${}^5_{\Lambda}\text{He}$  events from the E462 data. Since 30% beta decay electron events will be cut away in the data analysis, according to the GEANT4 simulation described above, we estimate the beta decay electron efficiency is 0.7. Considering these factors, we found that if  $29 \times 10^{12}$   $\pi^+$  enter a  $14\text{g/cm}^3$   ${}^6\text{Li}$  target, 673 counts of the beta decay electron can be obtained. Then the statical error will be  $\sim 3.8\%$ . When we assume that the number of  $\pi^+$  is  $3.0 \times 10^7/\text{spill}$  and the accelerator operation cycle is 5.2 second, the total beam time of  $5.5 \times 10^7$  second ( $\sim 1400$  hours) is needed.

Table 4.1: Expected yield of the  ${}^5_{\Lambda}\text{He}$  and its beta decay events estimated by the  ${}^5_{\Lambda}\text{He}$  yield measured in the KEK E462 experiment and a GEANT4 simulation.

Experiment	E462	Proposed experiment
Number of $\pi^+$ beam	$2.5 \times 10^{12}$	$29 \times 10^{12}$
${}^6\text{Li}$ target thickness	$3.70\text{ g/cm}^2$ (80 mm)	$14\text{ g/cm}^2$ (300 mm)
${}^5_{\Lambda}\text{He}$ counts after SKS analysis	45653	$2.0 \times 10^6$
$BR_{\beta}$		$8 \times 10^{-4}$
Pauli suppression effect		0.6
$e^-$ detection efficiency		0.7
Beta-ray counts		673

## 4.2 Yield and accuracy of lifetime

The lifetime of a  $\Lambda$  in  ${}^5_\Lambda\text{He}$  is measured by the same method as the KEK E462 experiment which measured the  ${}^5_\Lambda\text{He}$  lifetime with 4.0% statical accuracy. As written in Chapter 2, the lifetime of a  $\Lambda$  is measured by two timing counters around the Li target. One measures a timing of beam  $\pi^+$  just upstream of the target, and the other surrounding the target measures that of a proton from nonmesonic weak decay of  ${}^5_\Lambda\text{He}$ . To measure the decay time spectrum of the proton from  $\Lambda$ 's non mesonic weak decay ( $\Lambda p \rightarrow np$ ) within a 2.0% accuracy, as shown in Table 4.2, we need to measure the four times larger number of protons than the E462 experiment, assuming that the resolution of the timing counters and the accuracy of the track length measurement are the same or better than E462. Since, the branching ratio of  $\Lambda p \rightarrow np$  is much larger than that of the beta decay electron, this lifetime measurement does not need a long beamtime. If we request 120 hours beamtime, 4768 protons events can be detected, which satisfies the statistical error less than 2.0%.

Table 4.2: Expected yields of the  ${}^5_\Lambda\text{He}$  and proton events from their nonmesonic weak decay and the expected lifetime accuracy, estimated in comparison with the KEK E462 experiment.

Experiment	E462	Proposed experiment
Number of $\pi^+$ beam	$2.5 \times 10^{12}$	$2.5 \times 10^{12}$
${}^6\text{Li}$ target thickness	3.70 g/cm <sup>2</sup> (80 mm)	4.6 g/cm <sup>2</sup> (100 mm)
${}^5_\Lambda\text{He}$ counts after SKS analysis	45653	$5.7 \times 10^4$
$BR_p[16]$	0.28	0.28
proton detection efficiency		0.3
Proton counts	$\sim 1030$	4768
Time resolution (rms)	128 ps	128 ps
Statistical error of lifetime	4.0%	1.9%

## 5 Summary and future prospect

The possible modification of baryon structure in nuclear matter by the interaction between the quarks in the baryon and the meson field in nuclear matter has been discussed for a long time. Only the EMC effect indicates experimental evidence for baryon modification in nuclear matter, but its mechanism has not been clearly explained. To measure the modification caused by the meson fields, we propose an experiment for measuring the beta decay of  $\Lambda$  hypernuclei. The QMC (Quark Meson Coupling) model predicts that the axial charge  $g_A$  of a  $\Lambda$  reduces by 10% at maximum in nuclear matter, and the beta decay of a  $\Lambda$  reduces by 20% at maximum. To separate the baryon modification effects from nuclear many-body effects and hadronic effects, we plan to use a light hypernucleus,  ${}^5_\Lambda\text{He}$ . We expect that  ${}^5_\Lambda\text{He}$  hypernuclei will be produced via the  ${}^6\text{Li}(\pi^+, K^+) {}^6_\Lambda\text{Li}$ ,  ${}^6_\Lambda\text{Li} \rightarrow {}^5_\Lambda\text{He} + p$  reaction at J-PARC K1.1 beamline, and the beta decay rate will be determined with a 4.5% accuracy, by measuring the branching ratio and the lifetime determined with 4% and 2%, respectively.

In the measurement for the  $\Lambda$ 's weak decay lifetime, we will use the same setup as the KEK E462 experiment. We expect that the lifetime will be measured with less than 2% accuracy by measuring the time difference between the beam pion and the weak decay proton.

In the measurement of the branching ratio, a huge background of  $\pi^0$  and  $\pi^-$  from the  $\Lambda$ 's main decay modes should be reduced down to the order of 1% of the beta decay electron signal. For this purpose, we designed apparatus around the  ${}^6\text{Li}$  target made of plastic and lucite Cerenkov counters together with a BGO  $4\pi$  calorimeter and studied how to remove the background by simulation using the GEANT4 code. In the analysis for the BGO calorimeter, by selecting one-cluster hit events as the beta decay electron, 97% of  $\pi^0$  and 92.8% of  $\pi^-$  can be rejected. In the analysis for the plastic counter, by selecting a MIP peak region in the energy loss, 88% of  $\pi^0$  and 99.9% of  $\pi^-$  can be rejected. In addition, 95.5% of  $\pi^-$  and 90% of  $\pi^0$  events are rejected by the lucite Cerenkov counter. Via all the background suppression study, the background rate for the beta decay electron is found to be reduced down to 4%.

In the case of nonmesonic weak decay,  $\Lambda p \rightarrow np$  and  $\Lambda n \rightarrow nn$  events are found to be reduced well by the plastic counters and the lucite Cerenkov counters due to the low momentum of emitted  $nn$  and  $np$ . Finally,  $\Lambda p \rightarrow np$  and  $\Lambda n \rightarrow nn$  events are reduced to 2% and 4% of the beta decay electron signal.

In the case of quasi-free  $\Lambda$  (Q-F  $\Lambda$ ), the background rate for the beta decay electron is reduced down to 11.9%. In addition, by the cut of total energy loss in the BGO and the high theta number hit, the rate become 5.5%.

Roughly estimating, the systematic error of the background for the beta decay electron become  $\sim 5\%$  by subtracting the background within 30% accuracy.

Furthermore, we made simulations for optimization of the number of the BGO segments and the BGO thickness in order to reduce the preparing cost and the time. We found that the number of BGO segments should be larger than 100 because the analysis of cluster does not work well in the fewer BGO segments and the thickness should be larger than 20 cm, since more  $\pi^-$  events produce one cluster in the BGO for the smaller BGO thickness due to the reduction of the reaction rate of neutrons.

In addition, in order to detect leak photons from  $\pi^0 \rightarrow \gamma\gamma$  through the BGO downstream hole, the simulation for the photon veto counter to be installed around the SKS magnet was made. We found that by using two-layers structure ((5 mm lead and 5 mm plastic) $\times 2$ ), 64 % leak photon can be detected.

We also estimated the yield and accuracy for measuring the beta decay rate, and 1400 and 120 hours beamtime are found to be needed to achieve statistical errors of 4% and 2% for measuring the branching ratio and the lifetime. Therefore, we found that this beta decay experiment is found to be feasible.

In near future, we will make a more realistic background reduction simulation considering the energy resolution of BGO counters. Most of the present results have been reported in Letter-Of-Intent submitted to J-PARC [20]. After the detailed studies of the detectors by further simulations, we will write and submit a proposal of the experiment to the J-PARC PAC.

# Appendix A

## Beta decay

### A.1 Beta decay theory

The theory of the beta decay was constructed by Fermi in 1934. The probability of the beta decay  $w$  is given as

$$w = \frac{2\pi}{\hbar} |M_{if}|^2 \frac{dn}{dE_e}.$$

This is called Fermi's golden rule.  $M_{if}$  is the matrix element of the initial state and the final state of the nucleus and  $dn/dE_e$  is the density of states of the electron. The probability of the beta decay with the electron energy in the range  $E_e \sim E_e + dE_e$  is given as

$$w dE_e = \frac{g^2 |M_{if}|^2}{2\pi^3 \hbar^7 c^3} F(Z, p) E_e (E_0 - E_e)^2 \sqrt{E_e^2 - m_e^2} dE_e,$$

where  $g$  is the coupling constant.  $F(Z, p)$  is a factor of an effect from the Coulomb potential, and  $E_0$  is the sum of the  $Q$  value and the electron mass.

The decay probability  $\lambda$  is calculated by integrating as

$$\lambda = \int_{m_e}^{E_0} \frac{g^2 |M_{if}|^2}{2\pi^3 \hbar^7 c^3} F(Z, p) E_e (E_0 - E_e)^2 \sqrt{E_e^2 - m_e^2} dE_e = \frac{g^2 |M_{if}|^2}{2\pi^3 \hbar^7 c^3} f,$$

$$f = \int_{m_e}^{E_0} F(Z, p) E_e (E_0 - E_e)^2 \sqrt{E_e^2 - m_e^2} dE_e.$$

The half-life  $t$  is given as

$$t = \frac{\log 2}{\lambda} = \frac{\log 2}{\frac{g^2 |M_{if}|^2}{2\pi^3 \hbar^7 c^3} f},$$
$$\therefore ft = \frac{2\pi^3 \hbar^7 c^3}{g^2 |M_{if}|^2} \log 2.$$

This  $ft$  value is often used in the beta decay. By measuring the half-life  $t$  and by calculating  $f$ , and if we know the matrix element  $M_{if}$ , the coupling constant of the weak decay  $g$  is obtained. To calculate the matrix element, Hamiltonian density  $H_\beta$  should be considered. At first, Fermi gave

$$H_\beta = \frac{G_\beta}{\sqrt{2}} \left( l^\mu(x) N_\mu^\dagger(x) + N^\mu(x) l_\mu^\dagger(x) \right).$$

$G_\beta$  is the coupling constant of the beta decay.  $l^\mu$  and  $N_\mu^\dagger$  are the lepton and nucleon currents given as

$$l^\mu = \bar{\psi}_e(x) \gamma_\mu \psi_\nu(x), \quad N_\mu^\dagger = \bar{\psi}_p(x) \gamma_\mu \psi_n(x).$$

Therefore, Hamiltonian density is

$$H_\beta = \frac{G_\beta}{\sqrt{2}} (\bar{\psi}_e(x) \gamma^\mu \psi_\nu(x) \bar{\psi}_p(x) \gamma_\mu \psi_n(x) + \bar{\psi}_n(x) \gamma^\mu \psi_p(x) \bar{\psi}_\nu(x) \gamma_\mu \psi_e(x)).$$

In the  $\bar{\psi}_e(x) \gamma^\mu \psi_\nu(x) \bar{\psi}_p(x) \gamma_\mu \psi_n(x)$  part,  $\bar{\psi}_e, \bar{\psi}_p$  and  $\psi_\nu$  represent the generation of an electron, a proton and an anti-neutrino respectively.  $\psi_n$  represents extinction of a neutron. This part corresponds to  $\beta^-$  decay ( $n \rightarrow p e^- \bar{\nu}_e$ ).

The  $\bar{\psi}_n(x) \gamma^\mu \psi_p(x) \bar{\psi}_\nu(x) \gamma_\mu \psi_e(x)$  part corresponds to  $\beta^+$  decay ( $p \rightarrow n e^+ \nu_e$ ) and electron capture ( $p e^- \rightarrow n \nu_e$ ).

The matrix element  $M_{if}$  is given by

$$\begin{aligned} M_{if} &= \int d^3x \langle f | \bar{\psi}_e(x) \gamma^\mu \psi_\nu(x) \bar{\psi}_p(x) \gamma_\mu \psi_n(x) + \bar{\psi}_n(x) \gamma^\mu \psi_p(x) \bar{\psi}_\nu(x) \gamma_\mu \psi_e(x) | i \rangle \\ &= M_F. \end{aligned}$$

Here,  $|i\rangle$  and  $|f\rangle$  are the initial state and the final state of the nucleus, respectively. In this transition, the spin of the nucleus  $I$  does not change ( $\Delta I = 0$ ). In addition, the angular momentum  $J$  and the parity  $\pi$  also do not change. This beta decay is called ‘‘Fermi transition’’. If the spin of the nucleus changes in the beta decay,  $M_F$  becomes 0. Fermi’s Hamiltonian density above cannot describe the beta decay with  $\Delta I, \Delta J \neq 0$  and the change of the parity. Later, the beta decay with changes of the spin and the angular momentum was found, and it is called ‘‘Gamov-Teller transition’’. Therefore, the Hamiltonian density including both Fermi transition and Gamov-Teller transition were needed. Fermi’s Hamiltonian is composed of a scalar product of two vector currents to satisfy invariance under the Lorentz transformation. The lepton current and nucleon current should be four-vectors under the Lorentz transformation. For the types of the currents in the Hamiltonian, various types of currents such as  $\bar{\psi}\psi$  (Scalar),  $\bar{\psi}\gamma^\mu\psi$

(Vector),  $\bar{\psi}\gamma^\mu\gamma^\nu\psi$  (Tensor),  $\bar{\psi}\gamma^5\psi$  (pseudoscalar),  $\bar{\psi}\gamma^\mu\gamma^5\psi$  (Axial vector) (called as S, V, T, P, A, respectively) are allowed. Considering the invariance under the Lorentz transformation,  $H_\beta$  is expected to be made of coupling of S-S, V-V, T-T, P-P, S-P, V-A, A-A. Which current combination is correct was determined by experiments.

## A.2 Beta decay model under V–A

By experiments, the lepton and nucleon currents in the beta decay was found to be described as V – A. The Fermi's beta decay is described by Vector part of the nucleon current, and the Gamov-Teller's beta decay is described by Axial vector part of the nucleon current. Therefore, Hamiltonian density is given by linear combination of the vector and the axial vector nucleon currents as

$$H_\beta = \frac{G_\beta}{\sqrt{2}} [(\bar{\psi}_p\gamma_\mu\psi_n)(\bar{\psi}_e(C_V + C'_V\gamma_5)\gamma^\mu\psi_\nu) + (\bar{\psi}_p\gamma_\mu\gamma_5\psi_n)(\bar{\psi}_e(C_A + C'_A\gamma_5)\gamma^\mu\gamma^5\psi_\nu) + h. c. ],$$

where h.c. means Hermitian conjugate. Since the neutrino mass is regarded as 0 and the helicity of neutrino is negative,

$$C_V = C'_V, \quad C_A = C'_A \\ \frac{1}{2}(1 - \gamma_5)\psi_\nu = \psi_\nu, \quad \frac{1}{2}(1 + \gamma_5)\psi_\nu = 0.$$

Hamiltonian density is given by

$$H_\beta = \frac{G_\beta}{\sqrt{2}} [(\bar{\psi}_e\gamma^\mu(1 - \gamma_5)\psi_\nu)(\bar{\psi}_p\gamma_\mu(C_V - \gamma_5 C_A)\psi_n) + h. c. ].$$

Then,

$$|M_{if}|^2 = \left| \int d^3x \left\langle f \left| \frac{G_\beta}{\sqrt{2}} [(\bar{\psi}_e\gamma^\mu(1 - \gamma_5)\psi_\nu)(\bar{\psi}_p\gamma_\mu(C_V - \gamma_5 C_A)\psi_n) + h. c. ] \right| i \right\rangle \right|^2 \\ |M_{if}|^2 = C_V^2 M_F^2 + C_A^2 M_{GT}^2.$$

Therefore, the decay rate is

$$\Gamma_{beta} = \frac{G_\beta^2 |M_{if}|^2}{2\pi^3 \hbar^7 c^3} f = \frac{G_\beta^2 (C_V^2 M_F^2 + C_A^2 M_{GT}^2)}{2\pi^3 \hbar^7 c^3} f.$$

Here, the axial vector charge  $g_A$  and the vector charge  $g_V$  are defined as

$$g_A = C_A G_\beta, \quad g_V = C_V G_\beta$$

Finally, the decay rate is written as

$$\Gamma_{beta} = \frac{G_\beta^2 (C_V^2 M_F^2 + C_A^2 M_{GT}^2)}{2\pi^3 \hbar^7 c^3} f = \frac{g_V^2 M_F^2 + g_A^2 M_{GT}^2}{2\pi^3 \hbar^7 c^3} f,$$

and therefore,

$$\Gamma_{beta} \propto g_V^2 M_F^2 + g_A^2 M_{GT}^2.$$

### A.3 $g_V$ and $g_A$ values

In the quark and lepton level,  $g_V$  and  $g_A$  are  $g_V = 1$  and  $g_A = -1$ , respectively. In the hadronic level, a quark in the nucleon is affected via the strong interaction, and in fact, the axial charge  $g_A$  is changed in the nucleon. In contrast, the vector charge  $g_V$  is unchanged, and not affected by the hadronic effects. It is called Conserved Vector Current (CVC). The measurements for  $g_A$  and  $g_V$  of neutron in the free space were made and found to be  $g_A/g_V = -1.2724 \pm 0.0023$  [2].

The measurements for  $g_A$  and  $g_V$  of neutron in the nucleus was also made. The  $g_A$  value of neutron was found to be quenched in a nucleus as shown in Figure 2.1. For a light nucleus,  ${}^3\text{H}$ , quenching effect is  $\sim 5\%$ , but  $g_V$  is unchanged due to CVC.

## Appendix B

### J-PARC K1.1 beamline

#### B.1 J-PARC

J-PARC (Japan Proton Accelerator Research Complex) is a facility for studying nuclear and particle physics and material and life science. At J-PARC, by using high intensity proton beams, various secondary particles (ex. muon, neutron, neutrino, pion, and kaon) can be produced, and various experiments are carried out. Figure B.1 shows a schematic view of J-PARC. Linac (50 mA) accelerates protons to 400 MeV and Rapid Cycling Synchrotron (RCS) (333  $\mu$ A) accelerates protons to 3 GeV. Accelerated protons are transported to Material and Life Science Facility (MLF) and Main Ring (MR). They are accelerated to 30 GeV by MR (15  $\mu$ A) and transported to Hadron Experimental Facility.

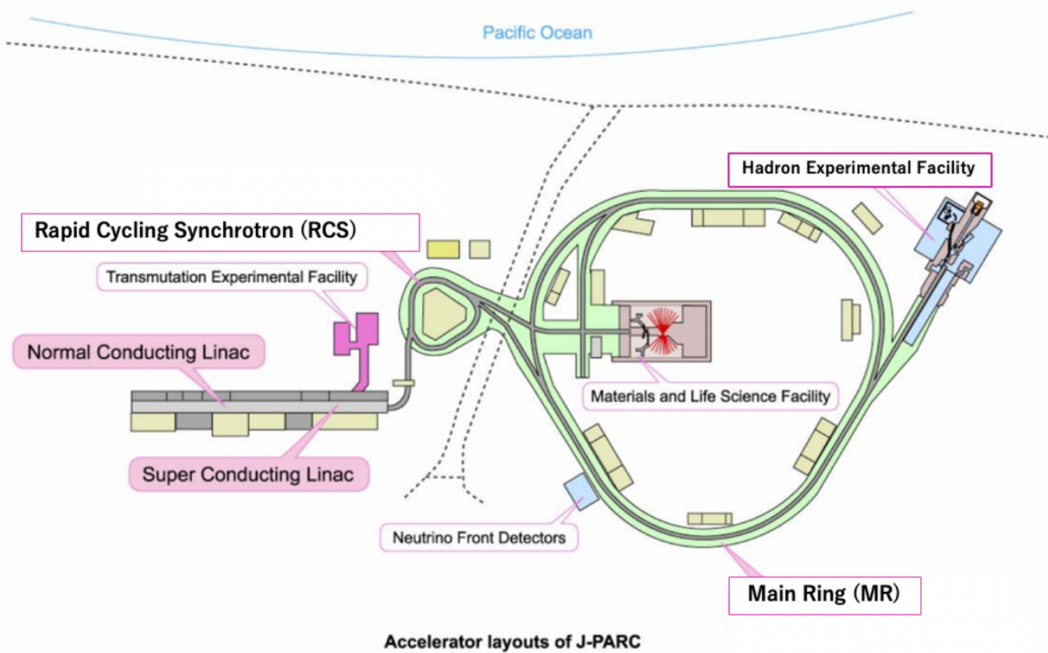


Figure B.1: A schematic view of J-PARC [23]. See text for details.

## B.2 J-PARC Hadron Experimental Facility

Figure B.2 shows a schematic view of the J-PARC Hadron Experimental Facility. Green shows the current beamlines, and orange shows beamlines planned to be constructed. At the Hadron Experimental Facility, 30 GeV protons are bombarded on the T1 target, then  $\pi$  and K mesons are produced, and they are transported to K1.8, K1.8BR and KL beamlines. A part of the protons are also transported to High-p and COMET beamlines.

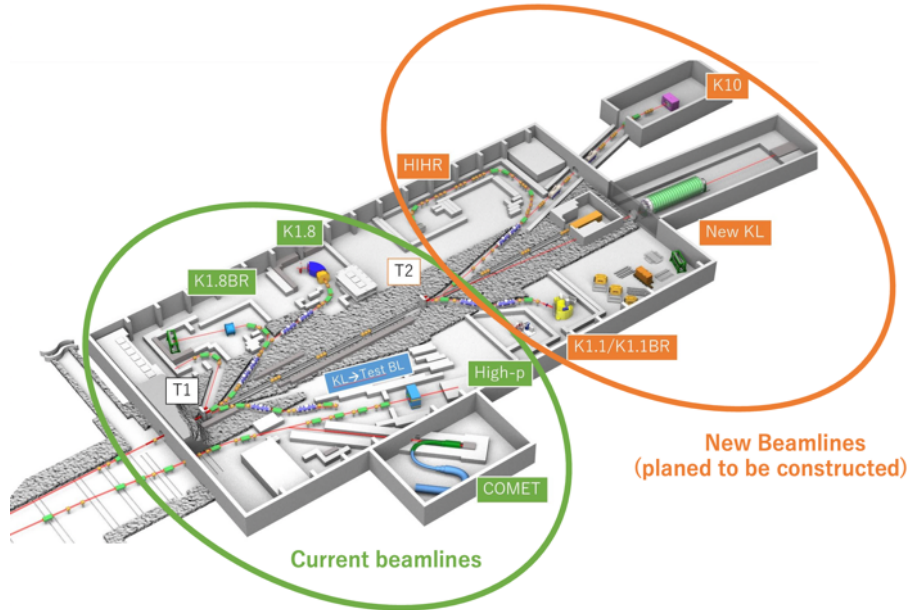


Figure B.2: A schematic view of the J-PARC Hadron Experimental Facility [24]. Accelerated protons are bombarded to the T1 target, and  $\pi$  meson, K meson and other particles are produced and transported to secondary beamlines.

## B.3 J-PARC K1.1 beamline

The K1.1 beamline is optimized for production of  $\Lambda$  and  $\Sigma$  hyperons ( $S = -1$ ). It will be constructed in near future in the current facility and then moved to the extended part of the facility. At the K1.1 beamline, the E63 experiment will be carried out. The E63 experiment will measure possible modification of the  $g$ -factor of a  $\Lambda$  in a nucleus, and the motivation is similar to the proposed beta decay experiment. Figure B.3 shows the overview of the K1.1 beamline. This beamline provides 1.05 GeV/c  $\pi^+$  beam suitable for  $\Lambda$  hypernuclear production with the expected intensity of  $\sim 3.0 \times 10^7 \pi^+/\text{spill}$ . However, produced particles from the T1 target include not only  $\pi^+$  but also other secondary particles and impurity particles. Impurity particles are produced due to decay

of secondary particles and interactions between beam particles and materials in the beamline. To increase purity of  $\pi^+$ , there are several devices such as IF, ESS, CM and MS.

The momentum of secondary beam particles is selected by dipole magnets (D1, D3) in the beamline. Intermediate focus point (IF) is designed to make the secondary beam particles focus but impurity particles not focus. After IF, two sets of electrostatic separators (ESS) are installed, and they separate particles with different velocities by electronic field. Compensation Magnets (CM) are installed in front of and behind each ESS, and they change focusing point of the beam particles. After ESS and CM, particles with a specific velocity, consequently with a specific mass, are selected by Mass Slit (MS). Finally, high purity  $\pi^+$  beam is transported to the K1.1 beamline spectrometer.

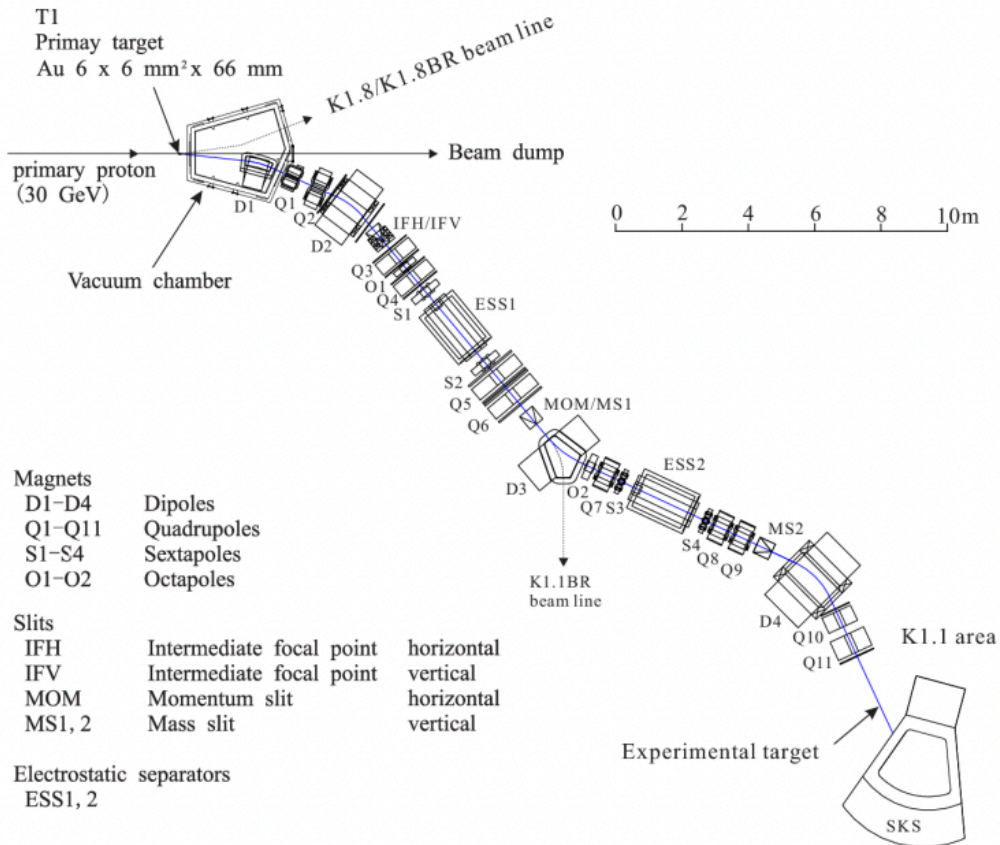


Figure B.3 A schematic view of the K1.1 beamline at J-PARC Hadron Experimental Facility [25].

## Appendix C

### The modification of $\Lambda \rightarrow n\gamma$ decay rate

#### C.1 $\Lambda \rightarrow n\gamma$ decay rate in nuclear matter

QMC model predicts that spatial distribution of u and d quarks is modified in a nucleus. This modification affects not only the beta decay rate but also the decay rate of  $\Lambda \rightarrow n\gamma$ . Figure C.1 shows the diagram of  $\Lambda \rightarrow n\gamma$  decay. When this decay occurs, an s quark changes to a u quark and a photon is emitted. We expect the decay rate of  $\Lambda \rightarrow n\gamma$  may also decrease. Although a calculation has not been done yet, we propose a measurement of the  $\Lambda \rightarrow n\gamma$  decay rate together with the beta decay rate measurement.

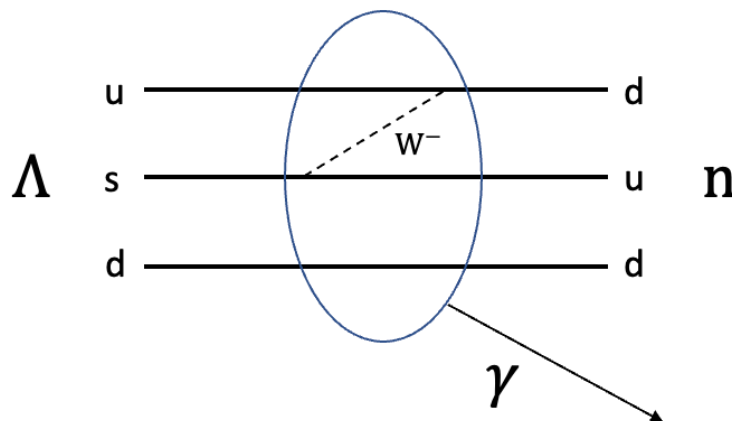
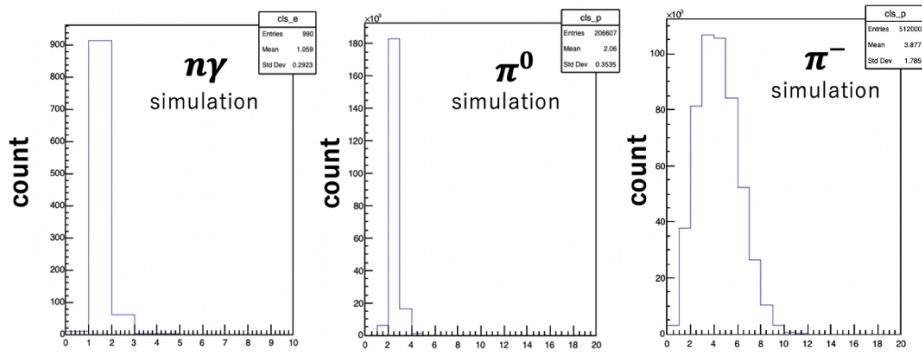


Figure C.1: A diagram of  $\Lambda \rightarrow n\gamma$  decay. In this decay, an s quark changes to a u quark, and a photon is emitted. Since the decay rate of  $\Lambda \rightarrow n\gamma$  depends on overlap of the initial state s quark wavefunction and the final state u quark wavefunction, the decay rate may decrease for the same reason as the beta decay.

The energy of the emitted photon from  $\Lambda \rightarrow n\gamma$  is calculated to be about 159.4 MeV considering the binding energy of  $\Lambda$  in  ${}^5_{\Lambda}\text{He}$  of  $\sim 3.1$  MeV [26]. We studied background rate for  $\Lambda \rightarrow n\gamma$  by GEANT4 simulation. In our simulation, a photon with 159.4 MeV is produced in random directions from the target, and  $\pi^0$  and  $\pi^-$  from  ${}^5_{\Lambda}\text{He}$  mesonic decay are produced as background in the same way as the background study for the beta decay electron measurement.

## C.2 Cluster analysis in the BGO calorimeter

When one photon from  $\Lambda \rightarrow n\gamma$  enters the BGO calorimeter, it is expected to produce one cluster. Figure C.2 shows the number of clusters in BGO. As shown here,  $\Lambda \rightarrow n\gamma$  produces one cluster in BGO, and  $\pi^0$  and  $\pi^-$  produce two and several clusters, respectively. By selecting one cluster events, 97% of  $\pi^0$  and 92.8% of  $\pi^-$  events are rejected.



The number of clusters in the BGO

Figure C.2 The number of clusters in the BGO for  $\Lambda \rightarrow n\gamma$ ,  $\pi^0$  and  $\pi^-$  in the simulation.

## C.3 Analysis in the plastic counters

Figure C.3 shows the total energy deposit in the plastic counter. As shown in Figure C.3, in the case of  $\Lambda \rightarrow n\gamma$  and  $\pi^0$ , the energy deposit mostly distributes under 0.2 MeV because a photon passes through. The energy distribution of  $\pi^-$  has a peak at 3 MeV. By

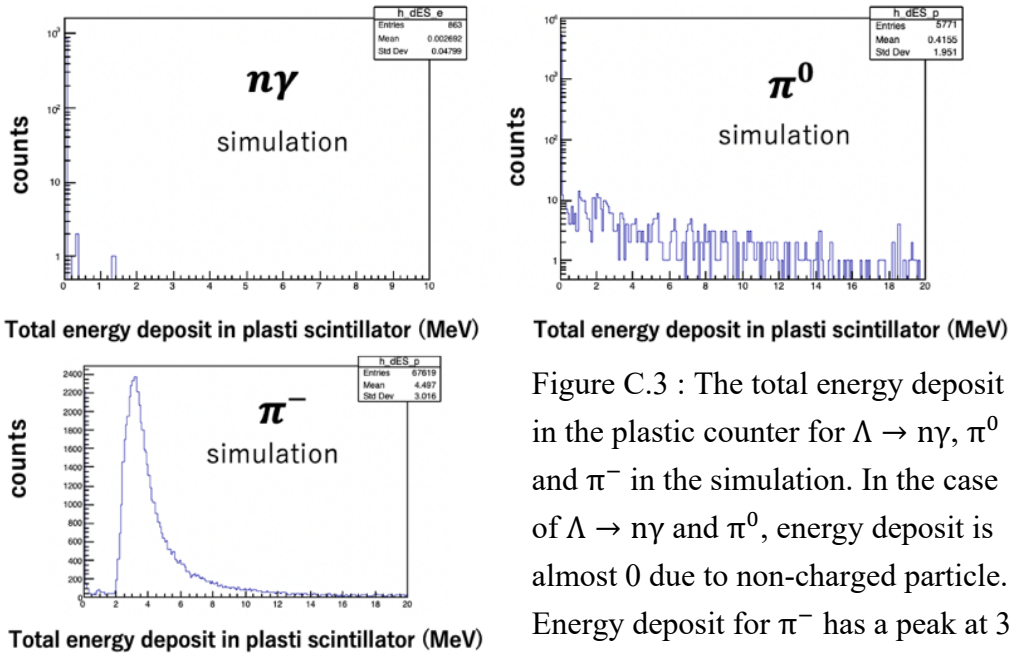


Figure C.3 : The total energy deposit in the plastic counter for  $\Lambda \rightarrow n\gamma$ ,  $\pi^0$  and  $\pi^-$  in the simulation. In the case of  $\Lambda \rightarrow n\gamma$  and  $\pi^0$ , energy deposit is almost 0 due to non-charged particle. Energy deposit for  $\pi^-$  has a peak at 3 MeV.

selecting  $< 0.2$  MeV events as  $\Lambda \rightarrow n\gamma$ , 96.5% of  $\pi^-$  events can be rejected.

## C.4 Analysis of the total energy deposit in BGO

Figure C.4 shows the total energy deposit of  $\Lambda \rightarrow n\gamma$ ,  $\pi^0$  and  $\pi^-$  in BGO after the analyses described above. As shown in Figure C.4, the  $\Lambda \rightarrow n\gamma$  spectrum shows a clear peak at 159.4 MeV. In the case of  $\pi^0$ , the total energy distributes at 30 – 140 MeV. This is because one photon from  $\pi^0 \rightarrow 2\gamma$  enters BGO and the other photon escapes from BGO. In the case of  $\pi^-$ , the energy widely distributes due to interaction between neutrons from  $\pi^-$  and nuclei in BGO. Via the background reduction above,  $\Lambda \rightarrow n\gamma$  events can be distinguished from  $\pi^0$  and  $\pi^-$  events by selecting energy around a 159.4 MeV peak. By selecting events with 143 MeV – 159.4 MeV in BGO as  $\Lambda \rightarrow n\gamma$ , 99.6% of  $\pi^0$  and 99.9% of  $\pi^-$  events are rejected. Figure C.5 shows a total energy spectrum of  $\Lambda \rightarrow n\gamma$  (blue) and  $\pi^0 + \pi^-$  (red). Via the analysis of the detectors, we can separate  $\Lambda \rightarrow n\gamma$  from background well. The background rate from  $\pi^0$  and  $\pi^-$  is about 0.24% of the  $\Lambda \rightarrow n\gamma$  signal. The reduction rate of  $\Lambda \rightarrow n\gamma$  events is about 15%. Statical error of the branching ratio of  $\Lambda \rightarrow n\gamma$  is expected to be about 3.4%.

## C.5 Summary

We studied accuracy for measuring the  $\Lambda \rightarrow n\gamma$  decay rate. Via the simulation, the background rate for the  $\Lambda \rightarrow n\gamma$  signal and the statical error of the branching ratio are found to be 0.24% and 3.4%, respectively. Therefore, measurements for  $\Lambda \rightarrow n\gamma$  together with beta decay is found to be feasible. In addition, the measurement of the  $\Lambda \rightarrow n\gamma$  decay rate is easier than that of the beta decay, if the BGO energy resolution is sufficient to separate the  $\Lambda \rightarrow n\gamma$  peak at 159.4 MeV from the  $\pi^0$  spectrum up to 140 MeV.

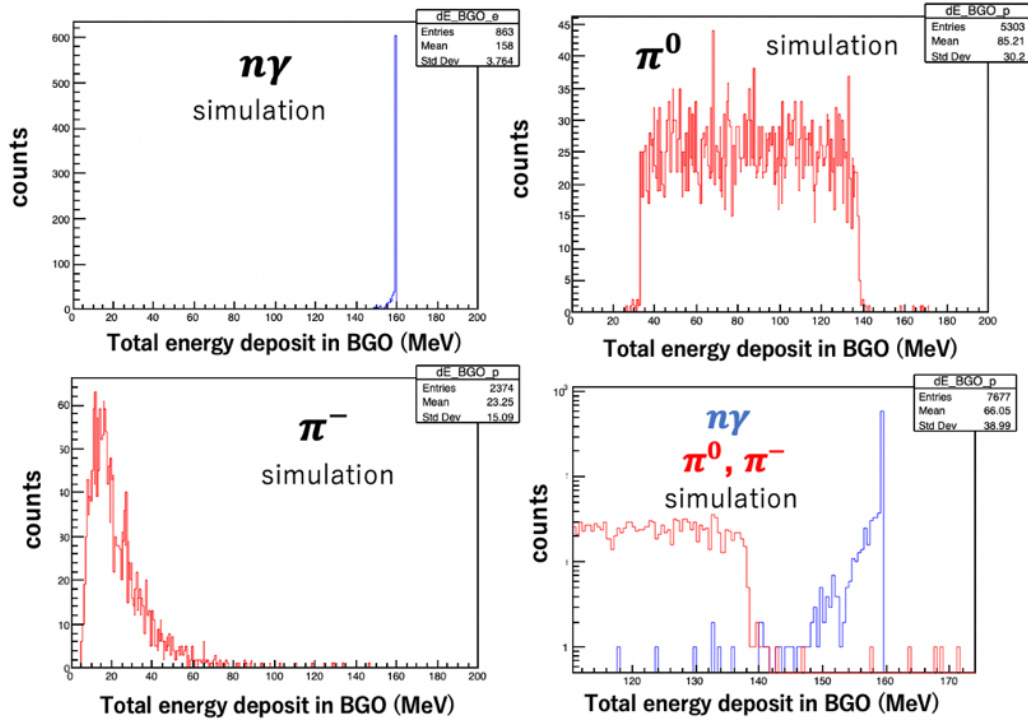


Figure C.4: The total energy deposit in the BGO for  $\Lambda \rightarrow n\gamma$ ,  $\pi^0$  and  $\pi^-$  in the simulation. The  $\Lambda \rightarrow n\gamma$  spectrum shows a clear peak at 159.4 MeV. For  $\pi^0$  and  $\pi^-$ , the BGO energy spectrum widely distributes. Right bottom figure shows the energy of  $\Lambda \rightarrow n\gamma$  (blue) and the main decay modes (red).

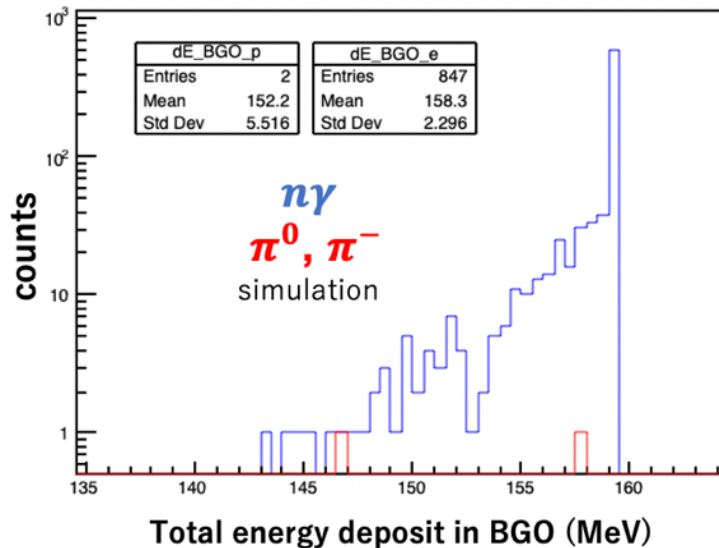


Figure C.5: Simulated energy spectrum of the photon from  $\Lambda \rightarrow n\gamma$  decay in the simulation. A clear photon peak from  $\Lambda \rightarrow n\gamma$  is seen, and the background level is extremely low. The background rate from  $\pi^0$  and  $\pi^-$  for the  $\Lambda \rightarrow n\gamma$  signal is about 0.24%.

# Reference

- [1] D. F. Geesaman, K. Saito, A. W. Thomas, *Ann. Rev. Nucl. Part. Sci.* 45 (1995) 337.
- [2] M. Tanabashi et al. (Particle Data Group), *Phys. Rev. D* 98, 030001 (2018)
- [3] P. A. M. Guichon, A.W. Thomas, *Phys. Lett. B*773 (2017) 332.
- [4] J.J. Szymanski et al., *Phys. Rev. C*43 (1991) 849.
- [5] S. Kameoka et al., *Nucl. Phys. A*754 (2005) 173c.
- [6] S. Okada et al., *Phys. Lett. B* 597 (2004) 249; S. Okada et al., *Nucl. Phys. A*754. (2005) 178c.
- [7] T. Motoba, H. Band.o, T. Fukuda, J. ˇZofka, *Nucl. Phys. A*534 (1991) 597.
- [8] I. Kumagai-Fuse, S. Okabe, Y. Akaishi, *Phys. Rev. C* 54 (1996) 2843.
- [9] K. Itonaga, T. Motoba, *Prog. Theor. Phys. Suppl.* 185 (2010) 252.
- [10] A. Parreno, A. Ramos, *Phys. Rev. C* 65 (2001) 015204.
- [11] C. Barbero, C. De Conti, A.P. Galeao, F. Krmpotic, *Nucl. Phys. A* 726 (2003) 267.
- [12] T. Motoba et al., *Nucl. Phys. A* 534 (1991) 597.
- [13] B.H. Kang et al., *Phys. Rev. Lett.* 96 (2006) 062301.
- [14] F. C. Khanna, I. S. Towner, H. C. Lee, *Nucl. Phys. A* 305 (1978) 349.
- [15] W. T. Chou et al., *Phys. Rev. C* 47 (1993) 163.
- [16] S. Kameoka, Ph.D. thesis, Tohoku University (2005).
- [17] R. Bertini et al., *Nucl. Phys. A*368 (1981) 365.
- [18] H. Tamura et al., *Phys. Rev. Lett.* 84 (2000) 5963.
- [19] H. Kanauchi, Master's thesis, Tohoku University (2018).
- [20] K. Kamada, M. Fujita, H. Tamura, Letter-Of-Intent to J-PARC (2021), [https://j-parc.jp/researcher/Hadron/en/pac\\_2107/pdf/LoI\\_2021-11.pdf](https://j-parc.jp/researcher/Hadron/en/pac_2107/pdf/LoI_2021-11.pdf)
- [21] T. Yamamoto, Ph.D. thesis, Tohoku University (2016).
- [22] J. Mougey et al., *Nucl. Phys. A*262, 461 (1976).
- [23] T. Katoh et al., 10th ICALEPCS Int. Conf. on Accelerator & Large Expt. Physics. Control Systems. Geneva, 10 - 14 Oct 2005, MO3.5-1O (2005).
- [24] K. Aoki et al., arXiv:2110.04462v1 [nucl-ex] 9 Oct 2021.
- [25] Y. Ishikawa, Master's thesis, Tohoku University (2019).
- [26] Satoshi N. Nakamura, *EPJ Web of Conferences*, 66 01020 (2014).

## 謝 辞

本研究を遂行するにあたり、多くの方々からご指導頂来ましたことに、心から感謝申し上げます。

指導教員である田村裕和教授には、物理学の基礎から、使用する検出器・シミュレーションの方法について、丁寧なご指導を賜り、多いに生かす事ができました。深夜のメールや突然の部屋への訪問においても、心よくお時間を取って熱心にアドバイスをして下さいました。誠にありがとうございました。これからも、実験のための proposal やその準備等において、これまで同様ご迷惑をおかけするかもしれませんが、何卒よろしく願いいたします。

JAEA の藤田真奈美博士研究員には、4年次の頃より、GEANT4 シミュレーションを始めるにあたって、プログラミングに疎かった私にコードの書き方から丁寧に教えて下さいました。藤田氏には感謝しても仕切れません。誠にありがとうございました。

中村哲教授、三輪浩司准教授、早川修平助教におかれては、多くの助言とご指導を賜り、大変お世話になりました。誠にありがとうございました。

東海村の J-PARC ハドロン実験施設への出張やミーティングの際には、JAEA の谷田聖氏、山本剛史氏、市川裕大氏、KEK の高橋俊行氏、鶴養美冬氏、東北大学の石川勇二氏、叶内萌香氏、京都大学の後神利志氏、原田健志氏、東京工業大学の滝鷹介氏、また J-PARC スタッフの皆様には、数々の助言を頂き、検出器・ハイパー核について丁寧に教えて下さいました。大変ありがとうございました。

坂尾珠和氏、梶川俊介氏にはシミュレーションでの不明点を教えていただき、GPPU 試験合格のための極意を教えていただき、その結果無事合格することができました。感謝申し上げます。また和田俊輔氏、北岡智真氏、大浦文也氏、森野泰斗氏には、ミーティングや東海村滞在中には大変お世話になりました。

最後に、本課程まで応援し続けてくれた家族、友人、本当にありがとうございました。

今後は、バリオンとクォークの階層構造解明に向け、研究に邁進してまいりますので、引き続きご指導とご協力を賜りますようよろしくお願いいたします。

令和4年2月10日

鎌田 健人